Sensitivity of nanocrystalline tungsten oxide to CO and ammonia gas determined by surface catalysts

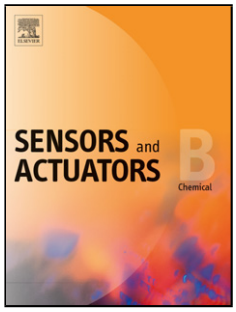

Title: Sensitivity of Nanocrystalline Tungsten Oxide to CO and Ammonia Gas Determined by Surface Catalysts

Authors: Artem Marikutsa, Lili Yang, Marina Rumyantseva, Maria Batuk, Joke Hadermann, Alexander Gaskov

PII: S0925-4005(18)31601-0
DOI: https://doi.org/10.1016/j.snb.2018.09.004
Reference: SNB 25310

To appear in: *Sensors and Actuators B*

Received date: 16-5-2018
Revised date: 22-8-2018
Accepted date: 2-9-2018

Please cite this article as: Marikutsa A, Yang L, Rumyantseva M, Batuk M, Hadermann J, Gaskov A, Sensitivity of Nanocrystalline Tungsten Oxide to CO and Ammonia Gas Determined by Surface Catalysts, *Sensors and amp; Actuators: B. Chemical* (2018), https://doi.org/10.1016/j.snb.2018.09.004

Sensitivity of Nanocrystalline Tungsten Oxide to CO and Ammonia Gas Determined by Surface Catalysts

*Artem Marikutsa * [a], Lili Yang [a], Marina Rumyantseva [a], Maria Batuk [b], Joke Hadermann [b], Alexander Gaskov [a]*

[a] Chemistry Department, Moscow State University, Vorobyevy gory 1-3, Moscow 119991, Russia

[b] EMAT, University of Antwerpen, Groenenborgerlaan 171, Antwerpen B-2020, Belgium

artem.marikutsa@gmail.com, roum@inorg.chem.msu.ru, maria.batuk@uantwerpen.be, joke.hadermann@uantwerpen.be, gaskov@inorg.chem.msu.ru

*Corresponding author. Tel: +7-495-9395471. Fax: +7-495-9390998. E-mail address: artem.marikutsa@gmail.com

Highlights

- Nanocrystalline tungsten oxide modified by Pd and Ru was obtained
- Effect of WO3 particle size and modification on surface sites is evaluated
- Blank WO3 interacts with the gases distinctly from the modified samples
- Sensing behavior of modified WO3 is determined by the catalytic additives
- Modification by Pd, Ru makes surface chemistry of different oxides similar

Abstract. Nanocrystalline tungsten oxide with variable particle size and surface area was synthesized by aqueous deposition and heat treatment for use in resistive gas sensors. Surface modification with 1 wt.% Pd and Ru was performed by impregnation to improve the sensitivity to CO and ammonia. Acid and oxidation surface sites were evaluated by temperature-programmed techniques using probe molecules. The surface acidity dropped with increasing particle size, and was weakly affected by additives. Lower crystallinity of WO_3 and the presence of Ru species favoured temperature-programmed reduction of the materials. Modifying WO_3 increased its sensitivity, to CO at ambient condition for modification by Pd and to NH_3 at elevated temperature for Ru modification. An in situ infrared study of the gas – solid interaction showed that the catalytic additives change the interaction route of tungsten oxide with the target gases and make the reception of detected molecules independent of the semiconductor oxide matrix.

Keywords. Tungsten oxide; chemical modification; gas sensor; carbon monoxide; ammonia; selectivity

1. Introduction

Although tungsten(VI) oxide attracts less attention as a resistive gas sensor than tin oxide, zinc oxide and titania [1], the chemistry of WO_3 is the most diverse among these metal oxide semiconductors (MOS). First, there is an abundance of polymorphic phases. The transformation between some polymorphs occurs at temperatures from 300 ^{0}C to above 500 ^{0}C, which coincides with the range of sensor operation temperatures [2-6]. Tungsten(VI) oxide further has a tendency towards oxygen deficiency, leading to the formation of the Magneli phase series (WO_{3n-1}, WO_{3n-2}) and specific individual compounds, e.g. $W_{24}O_{68}$, $W_{18}O_{49}$. Consequently, tungsten can exist in oxidation states lower than W(VI), i.e. W(IV) and W(V) [2, 7]. Therefore, due to intrinsic *n*-type semiconductor behavior (E_g = 2.6 eV [2]) favorable for chemisorption of acceptor molecules, WO_3 has often been used for NO_2 sensors [1, 8-10]. On the other hand,

because of high surface acidity, tungsten oxide has been widely applied for detection of ammonia [4, 5, 11-14]. Another promising application of WO_3-based sensors is monitoring nitrogen oxide and volatile organic compounds for breath analysis and medical diagnostics [15-21]. However, less is known on the chemical aspects of gas-solid interactions in these systems. This tendency holds on also for other types of sensing materials, including metal oxides, conducting polymers and novel two-dimensional materials and nanocomposites. Detection of inorganic gases is a suitable case study to find the ways to resolve the main issues of elevated operation temperature and poor selectivity of the metal oxide-based resistive sensors [22,23]. Regardless of the compositions of sensing layer, in-depth investigation of gas-solid interaction with metal oxides is of great necessity to unveil the underlying sensing mechanism, beneficial for extended molecular recognition of semiconducting metal oxides [24].

Sensing mechanisms of WO_3 were roughly classified into either the oxygen vacancy model focused on partial reduction of the oxide, or the model of oxygen ionosorption [1]. Regarding the latter, the interpretation of surface phenomena on tungsten oxide seems to be speculatively borrowed from the oxygen ionosorption model for tin oxide sensors [9, 13, 25]. There are few examples of dedicated experimental works on the surface chemistry of WO_3 sensors and more details on the gas-solid interactions would be useful [6]. Moreover, in these rare studies some peculiar transformations of bulk and surface WO_3 structure in the presence of particular gases (CO, NO_2, H_2S, water vapor) were revealed [6, 26, 27]. Nevertheless, in the present work we show that in definite cases the surface phenomena and sensing routes on WO_3 are similar to those on other *n*-type MOS. For oxides modified by Pd and Ru, the sensitization routes to CO and NH_3 gases provided by the catalytic additives are likely uniform for different MOS, including WO_3 and are based on the specific catalytic activity of noble metals in the oxidation of the target gas molecules.

This work aims to evaluate the effect of particle size and surface modification of nanocrystalline WO_3 on its active sites, sensing behavior and interaction with CO and NH_3 gases. The concept of chemical modification is based on the assumption that reception of particular gases is improved when noble metal additives with appropriate catalytic activity are supported on MOS, the latter serving as a transducer of electric response and as the source of adsorption sites, chemisorbed oxygen and OH-species [28-33]. Our previous research was focused on the chemical details of the gas-solid interaction, sensing processes and cluster-support interplay that demonstrated the adequacy of this model for Pd- and Ru-modified tin oxide [34-38]. The main findings were that Pd favored CO adsorption enabling its sensing at room temperature, and Ru catalyzed oxidation of ammonia to nitrogen oxides that improved sensitivity to NH_3 [38]. In this work, using sensing tests and in situ infrared spectroscopy we show that the interaction of the Pd- and Ru-modified WO_3 with CO and NH_3 is determined by the catalytic properties of the additives, reducing the distinction in surface chemistry between tungsten oxide and other MOS.

2. Materials and methods

Nanocrystalline tungsten(VI) oxide was obtained via aqueous deposition of tungstic acid followed by thermal treatment [39]. Ammonium paratungstate (APT, Sigma-Aldrich, >99% pure) was dissolved in water to obtain 16 mM solution. Nitric acid (7.8 M) was dropwise-added to the stirred APT solution at 80 ^{0}C, so that final concentrations in the mixture were 10 mM APT and 3 M HNO_3. The mixture was stirred at 80 ^{0}C for 30 min and for 1 h more while cooling to room temperature. The resultant yellow deposit of tungstic acid was centrifuged, washed with deionized water and dried at 80 ^{0}C overnight. The dried residue was separated into four parts, which were annealed for 24 h at different temperatures: 300, 450, 600, 800 ^{0}C.

The obtained WO_3 samples with different microstructure parameters were modified by 1 wt.% of Pd or Ru via impregnation. WO_3 powders were dispersed in ethanol solutions

of $Pd(acac)_2$ or $Ru(acac)_3$, and the solvent was evaporated under heating and stirring. The residual $WO_3/Pd(acac)_2$ and $WO_3/Ru(acac)_3$ powders were annealed for 24 h at 225 ^{0}C and 265 ^{0}C, respectively, to decompose noble metal precursors.

The X-ray powder diffraction was measured with a DRON-3M diffractometer, Cu Kα radiation. Specific surface area was evaluated by nitrogen adsorption within the Brunauer-Emmett-Teller (BET) model, in single-point measurement mode using a Chemisorb 2750 (Micromeritics) instrument with thermoconductivity detector. X-ray fluorescence (XRF) microanalysis was performed with a Mistral M1 (Bruker) spectrometer at an X-ray source operating voltage of 50 kV, current 800 mA, and diameter of scanned area 1.5 mm. TEM images and electron diffraction were registered using a FEI Tecnai G2 microscope operated at 200 kV. High angle annular dark field scanning transmission electron microscopy (HAADF-STEM) images and energy dispersive X-ray (EDX) maps were acquired using a FEI Osiris microscope equipped with a Super-X detector and operated at 200 kV. The materials were mixed with ethanol using an ultrasonic bath and deposited onto a Cu TEM grid covered with holey carbon. Temperature-programmed reduction (TPR) with hydrogen was performed on a Chemisorb 2750 (Micromeritics) instrument. The samples (30 mg) were pretreated under dry air flow at 200 ^{0}C for 1 h to clean the surface from adsorbed impurities and cooled to room temperature. TPR was registered under flow of H_2 (10 %) in Ar and heating to 900 ^{0}C with rate 5 ^{0}C/min. Temperature-programmed desorption (TPD) of ammonia was also measured on the same device. Granulated powders (100 mg, fraction 0.25 – 0.50 mm) were pretreated at 200 ^{0}C in He (30 ml/min) for 1 h, then in pure air for 1 h more, and cooled to room temperature. Samples were saturated under flow of NH_3 (8 %) in He for 1 h, then degassed under He flow at 50 ^{0}C for 20 mins to remove physisorbed ammonia. Desorption into He (30 ml/min) was measured on heating to 800 ^{0}C with rate 10 ^{0}C/min. X-ray photoelectron spectroscopy (XPS) of supported Pd and Ru species was recorded with Axis Ultra DLD (Kratos, UK) spectrometer with Al K_α source; binding energy was calibrated by C1s at 285.0 eV. Fourier-transformed infrared (FTIR) spectra and diffuse-

reflectance infrared Fourier-transformed (DRIFT) spectra were registered by Frontier (Perkin Elmer) spectrometer. FTIR spectra were recorded in 4000 – 400 cm^{-1} region using KBr pellets. DRIFT spectroscopy was performed using a DiffusIR annex and heated flow chamber HC900 (Pike Technologies) sealed by ZnSe window. DRIFT spectra were registered in the 4000 – 1000 cm^{-1} region with resolution 4 cm^{-1} and with accumulation of 30 scans at ambient conditions with automatic H_2O/CO_2 compensation. Powders (30 mg) were placed in alumina crucibles (5 mm diameter). Measurements were performed from samples exposed to a flow of 100 ml/min of CO (200 ppm) in air at 30 ^{0}C, and NH_3 (200 ppm) in air at 30 ^{0}C and at 200 ^{0}C. Prior to measurement, the samples were heated under purified air flow at 200 ^{0}C to remove the adsorbed impurities.

Sensor measurements were performed with a PC-controlled 4-sensor electrometer equipped with a flow chamber. Samples were dispersed in terpineol and the paste was drop-deposited onto alumina substrates embedded in TO-8 package and provided with Pt contacts (0.3×0.2 mm, gap 0.2 mm) and Pt-heaters. Sensors were heated at 200 ^{0}C for 20 h to remove the binder. The formed sensing layer was about 1×0.5 mm^2 in area and about 10 μm thick. DC-resistance was measured at applied voltage 1.3 V under gas flow 100 ml/min at fixed temperature in the range 25 – 200 ^{0}C. Background gas was purified air from a generator of pure air model "1,2-3,5" (Himelectronica, Russia), with contamination levels within the limits of 10 ppm H_2O, 2 ppm CO_2, 0.1 ppm hydrocarbons. Sources of test gases were bottled certified gas mixtures of NH_3 (1100 ± 20 ppm) in N_2 and CO (1250 ± 25 ppm) in N_2 (MGPZ, Russia). Dilution and concentration control on the level 1 – 100 ppm was realized by EL-FLOW mass-flow controllers (Bronkhorst). Humidity of the carrier gas was controlled by mixing two flows of pure air with different flow rates: the dry one from the source and the humid one purged through a bubbler which was filled by deionized water. All measurements were performed under steady relative humidity level (room temperature), that was verified using a humidity meter IVTM-7K (Eksis,

Russia). The sensor signal (hereafter also referred to as sensitivity) was defined as a ratio of sensor resistance in air (R_a) to that in the presence of the test gas (R_g):

$$S = R_a/R_g \qquad (1).$$

Response and recovery times were determined as the time needed for sensors to reach 90% of steady resistance value after the start (i.e. R_g/0.90) and the stop (0.90R_a) of exposure to a target gas, respectively.

3. Results and discussion

3.1. Composition and microstructure of samples

The list of synthesized samples, their composition and microstructure parameters is given in Table 1. According to XRD (Fig. 1) and electron diffraction (insets in Fig. 2*a*,*b*), the obtained samples constitute the nanocrystalline monoclinic γ-WO_3 phase, which is the polymorph stable at room temperature and up to 304 – 330 ^{0}C [3, 6]. When increasing the annealing temperature from 300 to 800 ^{0}C, the particle size (d_{XRD} calculated by Scherrer equation) of WO_3 increased and the BET area accordingly decreased (Table 1). Modification by Pd or Ru had no effect on the tungsten oxide crystallinity: the XRD peak positions (Fig. 1) and microstructure parameters were the same within the measurement errors (Table 1).

TEM and HAADF-STEM images demonstrate WO_3 synthesized at 300 ^{0}C (Fig. 2*a*, *c*). The WO_3 particles are severely agglomerated and have close orientation, which results in a diffraction pattern resembling that of single crystals (inset in Fig. 2*a*). Nevertheless, the individual nanoparticles of a size 5-10 nm can be clearly seen at the edges of the agglomerates (few individual particles are indicated by arrows) confirming the results of XRD. With increasing of the synthesis temperature to 450 ^{0}C, the size of WO_3 crystals considerably increase and varies from 10 to 200 nm (Fig. 2*b*,*d*).

The noble metal additives were observed by STEM-EDX mapping. Palladium was mainly present in the form of spherical nanoparticles, ranging from 3 to 14 nm in diameter for those observed, independent of the particle size of the tungsten oxide support (Fig. 2*e*). Ruthenium nanoparticles had a less pronounced shape; the observed particles varied in size from 5 to 12 nm in the WO_3-450/Ru sample (Fig. 2*f*). In the WO_3-300/Ru sample, ruthenium was only found in the form of RuO_2 crystals with a size of a few hundred nm.

The concentration of additives in WO_3/Pd, WO_3/Ru measured by XRF agreed with the loaded one (1 wt.%). XPS spectroscopy showed that in WO_3/Pd palladium was in Pd^{2+} and Pd^0 valence states, with the relative amounts Pd^{2+}:Pd^0 = 4.5:1 (Fig. 3*a*). The Ru^{4+} state like in RuO_2 was found in the WO_3/Ru samples (Fig. 3*b*). The observed oxidation state of Pd and Ru is coincident with that previously shown for tin oxide-based nanocomposites [40].

3.2. Surface species of WO_3 in relation to microstructure and surface modification

The FTIR transmission spectra of the samples are dominated by the broad tungsten-oxygen band of the WO_3 lattice (500 – 1000 cm^{-1}, Fig. 4). It covers the wavenumber range of stretching vibrations of W=O (950 cm^{-1}) and W-O-W bonds in octahedral edge-sharing and corner-sharing locations (800 – 650 cm^{-1}) [41, 42]. Surface H_2O and OH-species were detected by the bands of stretching O-H (3400 cm^{-1}) and bending H_2O (1620 cm^{-1}) and W-OH vibrations (1410 cm^{-1}) [43]. As inferred from Fig. 3*a*, the highest population of aqueous species on the surface of pristine WO_3 was found on WO_3-300 in accordance with the least particle size and largest BET area of this sample. Its modification resulted in weaker OH, H_2O and W-OH peaks for WO_3/Pd and the absence of these peaks on the spectrum of WO_3/Ru, possibly due to the additional thermal treatment after the impregnation procedure. A stronger depletion of aqueous species was found for tungsten oxide synthesized at higher temperatures (Fig. 4*b,c*). It should be due to smaller surface area available for water chemisorption. Yet, the spectra of samples based on WO_3-800 have a high background in this wavenumber region due to IR absorption by free charge carriers in the semiconductor grains (Fig. 4*d*).

To determine the oxidative surface species, thermoreduction with hydrogen was measured. The TPR profiles demonstrate the H_2 absorption rate dependence on temperature (Fig. 5). The major peak arising above 600 ^{0}C is due to WO_3 bulk reduction, since its total area corresponds to a stoichiometric molar ratio of H_2:WO_3 ≈ 3:1. Moreover, it could be resolved into lower-temperature (T_1 = 600 – 700 ^{0}C) and higher-temperature (T_2 = 700 – 900 ^{0}C) parts, their areas related as about 1:2. Thus, as temperature increased, tungsten(VI) oxide was likely reduced to WO_2 (eq. 2) and after that – to tungsten metal (eq. 3):

$$WO_{3(s)} + H_{2(g)} = WO_{2(s)} + H_2O_{(g)}, \quad \text{at } T_1 \qquad (2);$$

$$WO_{2(s)} + 2\ H_{2(g)} = W_{(s)} + 2\ H_2O_{(g)}, \quad \text{at } T_2 \qquad (3).$$

The bulk reduction maxima of WO_3 shifted to higher temperatures with the increase of particle size, most prominently for the sample obtained at 800 ^{0}C (Fig. 5*a*). It is reasonable to propose that the oxide lattice stability improved with the growth of the crystallites. However, it was not the case for modified tungsten oxide. Bulk reduction maxima of WO_3/Pd and WO_3/Ru (T_1 = 610 – 660 ^{0}C, T_2 = 740 – 800 ^{0}C) were shifted to lower temperature than for the pristine samples, and their positions had no dependence on the particle size of the tungsten oxide matrices (Fig. 5*b*,*c*). It can be due to the catalytic action of the noble metal clusters in the reactions (2, 3), e.g. via hydrogen spillover and/or promotion of oxygen exchange in the supporting oxide [40]. H_2 consumption at 130 – 200 ^{0}C was detected by WO_3/Ru samples (Fig. 5*c*). Assuming that it was due to the reduction of RuO_2, the consumed H_2 amount would correspond to a concentration of ruthenium 3 – 5 times exceeding the actual Ru content. Since WO_3/Ru had least surface hydroxyl contents (FTIR data, Fig. 4*a*), this peak is attributable to the reduction of chemisorbed oxygen species:

$$O_{2(ads)} + 2\ H_{2(g)} = 2\ H_2O_{(g)} \qquad (4).$$

The concentration of $O_{2(ads)}$ species evaluated from TPR was about 10 – 14 micromole/m^2 on WO_3-300/Ru; the quantification for other samples was hampered by a large uncertainty in the values of the BET area. The additive likely facilitates oxygen chemisorption on the oxide

surface, similar to the effect reported for Ru-modified tin oxide [36, 40]. The attribution of surface oxidative sites to diatomic oxygen species is conditional here, based on the model of temperature-dependent adsorbate types for other *n*-type MOS [44].

The surface acidity of pristine tungsten oxide was analyzed by thermodesorption of ammonia probe molecules. Because of catalytic action of Pd and, especially, of Ru additives, NH_3 oxidation was significant at raised temperature and desorption could not be reliably measured from the modified samples. Acid sites were identified and quantified using the TPD model from ref. [45]. TPD profiles demonstrated continuous NH_3 desorption on heating of WO_3 at 80 – 500 ^{0}C (Fig. 6*a*). Although ambiguous, we divided the TPD profiles into temperature ranges corresponding to desorption from weak (Broensted) acid sites (below 200 ^{0}C) and from Lewis sites of medium (200 – 400 ^{0}C) and strong acidity (above 400 ^{0}C). The Broensted sites represent surface OH-groups and the Lewis sites are surface cations with an incomplete coordination environment. The concentration of acid sites decreased following the coarsening of the WO_3 microstructure (Fig. 6*b*); for WO_3-800 the concentration could not be evaluated. The exceptionally high Lewis acidity of WO_3-300 could be due to defect cationic sites. At higher synthesis temperature, the growth and sintering of oxide grains made them less defective and exposed a smaller number of coordinately unsaturated cations.

3.3. Sensitivity to CO and NH_3 gases

The dynamic response to 20 ppm of CO and NH_3 in dry air is illustrated in Fig. 7. Raw data for other sensors and measurement conditions are given in the Supplementary data.

The overview of sensitivity to CO and NH_3 as a function of operating temperature is summarized in Figs. 8, 9. For convenience, the sensor signals are plotted as a logarithmic function lg*S*, so that positive lg*S* indicates an *n*-type response to the reducing gas, while negative lg*S* implies a *p*-type response. All sensors responded to CO as typical *n*-type MOS (positive lg*S* in Fig. 8, dynamic response in the Supplementary data). In contrast to almost insensitive pristine and Ru-modified tungsten oxide, the samples WO_3/Pd displayed improved CO sensitivity with

the maximum response at room temperature (Fig. 8). Thus, the major effect on CO sensitivity was due to sensors composition, i.e. the presence of Pd modifier, which is rationalized by DRIFT spectroscopy to be due to specific chemisorption of target molecules (Section 3.4). The influence of materials microstructure on CO sensitivity was as well prominent. The signals were higher for the sensor WO_3-300/Pd based on tungsten oxide with lowest particle size and largest surface area (Table 1). With respect to the surface species composition discussed above, the higher CO sensitivity is consistent with the larger concentration of OH-groups and chemisorbed oxygen species on the samples synthesized at 300 ^{0}C. These surface sites are responsible for oxidation of chemisorbed CO molecules, as discussed below (eq. 6). The response and recovery times were 4 min and 30 min, respectively (Fig. 7*a*). The discrepancy between fast response and slow recovery might be assigned to facile CO chemisorption on Pd sites during the exposure stage and its poor desorption back in air from the unheated sensor surface, as inferred from the DRIFT results.

The response of WO_3 and WO_3/Pd sensors to ammonia gas behaved as *n*-type at an operating temperature higher than 100 ^{0}C and switched to *p*-type at lower temperature (negative lg*S* in Fig. 9; dynamic response in the Supplementary data). The unusual *p*-type response of tungsten oxide to NH_3 has been observed elsewhere and was assigned to high oxygen deficiency or inversed surface conduction in fully depleted narrow nanowires [14, 46]. Resistance increase may be related to the fact that at low temperature the main interaction route was NH_3 chemisorption on acid sites of the WO_3 surface, as inferred by TPD (Fig. 6) and DRIFT (Fig. 13). The trend of the *p*-type signal values at 50 ^{0}C for pristine WO_3 coincides with the increase of BET area and surface acidity. Modification by Ru brought about high sensitivity to NH_3 with an *n*-type response in the whole tested operating temperature range. The largest signals were measured for the sensor based on WO_3-450/Ru operated at 200 – 250 ^{0}C (Fig. 9). Noteworthy, this sample had moderate BET area among the WO_3/Ru series, i.e. the effect of the microstructure on the sensitivity to reducing gases was not as expected. That the highest sensor signals were observed

not on the sample with larger surface area may be ascribed to high surface acidity of the WO_3-300 based samples (Fig. 6*b*). It leads to strong acid-base interaction with NH_3 preventing the bound target molecules from the redox conversion necessary for sensor response formation. Due to the elevated temperature, the response and recovery time was short, i.e. 1 min for response and 4 min for recovery (Fig. 7*b*). Thus, WO_3 modification by catalytic additives yielded materials with improved sensitivity: WO_3/Pd to CO at room temperature and WO_3/Ru to NH_3 at about 200 ^{0}C. This sensitization effect is similar or even exceeding that previously observed for SnO_2- and In_2O_3-based sensors (Fig. 10). The sensor signals for the optimized nanocomposites are linearly dependent on the concentration of the target gas (2 – 100 ppm) in logarithmic scale. With the increase of relative humidity (RH) of the gas flow, the sensor signals decreased (Fig. 11). Most abrupt drop was in case of room temperature CO detection by WO_3/Pd. Extrapolating the linearized dependences to S = 1 (the absence of sensor signal), the detection limits of CO were found to increase from ~1 ppm (in dry air) to ~10 ppm (13% RH) and ~20 ppm (21% RH), while under 30% RH and higher humidity it could not be detected by WO_3/Pd at room temperature (Fig. 11*a*). However, due to raised operation temperature of appropriate ammonia sensing (200 ^{0}C) the signals of WO_3/Ru to this analyte were not so drastically interfered by humidity. The lowest tested concentration 2 ppm NH_3 was reliably detected by WO_3/Ru even under 90% RH (Fig. 11*b*).

For the estimation of sensors selectivity, the sensor signals to fixed concentrations (10 ppm) of different inorganic gases are compared in Fig. 12. The signals were measured at the appropriate operation temperature of the sensors: bare WO_3 – at 300 ^{0}C, WO_3/Ru – at 200 ^{0}C and WO_3/Pd – at room temperature. Although the analytes tested include the reducing gases as well as oxidizing ones (NO_x), it can be seen that blank WO_3 had comparable sensitivities to H_2S and NO_2. On the other hand, WO_3/Pd was sensitive only to CO at room temperature. The Ru-modified sensor demonstrated highest sensor signals to ammonia with low cross-sensitivity to H_2, SO_2 and NO_x (Fig. 12).

3.4. DRIFT study of the interaction with CO and NH_3 gases

DRIFT spectra of pristine and modified tungsten oxide interacting with CO at room temperature are shown in Fig. 13. No spectral changes were observed for WO_3 and WO_3/Ru, in agreement with the lack of CO sensitivity of these samples. On the contrary, the spectra of Pd-modified samples demonstrated clear signs of chemical interaction. The intensity of the observed peaks correlated with the increase of BET area of WO_3/Pd samples. The main features were: a) increased background due to absorption by free charge carriers, indicating electronic transfer to tungsten oxide as a result of CO oxidation; b) appearance of C-O stretching vibrational peaks in the region (2150 – 1950 cm^{-1}) of carbonyl groups; c) depletion of IR adsorption at the vibrational frequencies of aqueous species, i.e. O-H (3450 – 3000 cm^{-1}), H_2O (1620 cm^{-1}) and W-OH (1410 cm^{-1}). Different modes of CO chemisorption could be distinguished from the carbonyl bands. CO binding to oxidized and reduced palladium sites in terminal conformation was revealed from the peaks at 2150 cm^{-1} (Pd^{2+}-CO) and 2115 cm^{-1} (Pd^{+}-CO) with a shoulder at 2090 cm^{-1} (Pd^{0}-CO) [47]. The peak at 1960 cm^{-1} is indicative of Pd-bound bridging carbonyls.

Red shift of vibrational frequency from that in free molecules (2143 cm^{-1}) is caused by π-donation from Pd to CO antibonding orbital, which loosens the C-O bond. Notably, the relative intensity of the peaks of bridging (1960 cm^{-1}) vs. terminal (2090 – 2150 cm^{-1}) carbonyls steeply increased on the spectra from WO_3-600/Pd to WO_3-300/Pd (Fig. 13). That the sensitivity increased in this sequence suggests that it was controlled by the strength of CO chemisorption on Pd sites, although the effect of larger BET area is in line as well. The negative bands of H_2O and OH-groups cannot be ascribed to competitive CO adsorption. Desorption of chemisorbed water usually needs thermal activation and is unlikely to take place at room temperature. Hence, the interaction of hydroxyl species with chemisorbed CO can be suggested as a reason for OH-groups depletion. It does not rule out the possible participation of surface oxygen species in sensor response formation, as is often proposed but hard to prove experimentally [13, 25]. Thus,

we propose that the route of room temperature CO oxidation on WO_3/Pd includes the following key steps:

a) chemisorption $CO + Pd = Pd\text{-}CO$ (5);

b) oxidation $Pd\text{-}CO + OH = Pd + CO_2 + H^+ + e^-$ (6).

DRIFT spectra in the presence of ammonia were registered so as to compare its adsorption at room temperature (Fig. 14) and reaction at 200 ^{0}C (Figs. 14, 15) with samples having different composition and microstructure. The adsorption was higher on WO_3-300 based materials in accordance with the larger BET area and higher concentration of acid sites on these samples. The adsorption of ammonia resulted in the appearance of bending bands of NH_4^+ (1450 cm^{-1} [48]) and NH_3 (1220 cm^{-1}, 1280 cm^{-1} [49, 50]) due to ammonia bound with hydroxyl and cation sites, respectively, and stretching N-H vibrational band at 3170 – 3320 cm^{-1}. The adsorption on Broensted acid sites accounts for depletion in stretching O-H (3650 – 3400 cm^{-1}) and bending H_2O (1620 cm^{-1}) regions. The interference with the negative W-OH peak (1415 cm^{-1}) may be the reason for NH_4^+ peak splitting. The composite structure of the ammonia-related bands might be due to the occurrence of several types of NH_3, NH_4^+ species. These can arise from binding to surface sites with diverse acid strengths, the higher wavenumber corresponding to stronger acidity [49]. Modification by Pd or Ru had minor influence on NH_3 adsorption at room temperature, unlike the effect of the tungsten oxide microstructure. The adsorption declined significantly on samples with lower BET area (Fig. 14).

The spectra of pristine WO_3 interacting with NH_3 at 200 ^{0}C still displayed the traces of ammonia adsorption, i.e. multiple positive N-H peaks at 3250 – 3390 cm^{-1} and NH_3 peaks at 1220 cm^{-1}, 1290 cm^{-1} (Fig. 15*a*), as well as negative bands of aqueous surface species at 3650 – 3400 cm^{-1} and 1620 cm^{-1}. However, these bands were much weaker than at room temperature and decreased with the BET area of WO_3, except the sharp peak at 1220 cm^{-1} on the spectrum of WO_3-600 ascribable to NH_3 adsorbed on Lewis acid sites of medium strength. The main features were the growth of the background absorption due to the increasing concentration of free

electrons yielded by NH_3 oxidation. The negative broad bands at 2060 cm^{-1} and 1850 cm^{-1}, identified as overtone peaks of W-O vibrations, imply the partial reduction of tungsten oxide [6, 26]. Actually, these peaks were also present on the spectra of WO_3-300 and, more prominently, of WO_3-450 already at room temperature (Fig. 14). The interaction with NH_3 proceeded essentially differently on modified tungsten oxide (Fig. 15*b*,*c*). The spectra of WO_3-300/Pd and WO_3-300/Ru samples were dominated by the bands of adsorbed ammonia species, mainly stretching N-H (3200 cm^{-1}) and bending bands of NH_3 (1290 cm^{-1}, 1220 cm^{-1}) and NH_4^+ (1410 cm^{-1}). The latter was shifted to lower wavenumber, in comparison to room-temperature adsorbed NH_4^+ (Fig. 14), and coincided with the position of bending W-OH vibrations. However, it cannot be due to hydroxyl species, since the other bands of aqueous species were negative (3650 – 3400 cm^{-1}, 1620 cm^{-1}). Neither background shift, nor W-O overtone peaks were observed for modified samples. The difference with pristine tungsten oxide is even larger on the spectra of WO_3-450-based materials (Fig. 15*c*). The background IR absorption did not change during the interaction of WO_3/Pd and WO_3/Ru with ammonia. It can be due to electronic depletion of semiconductor particles brought about by supported clusters, which agrees with higher resistance of the modified tungsten oxide sensors (resistance data in the Supplementary data).

The main distinctive feature on the spectra of WO_3/Ru (Figs. 14*b*,*c*, 15) is the evolution of the peak at 1860 – 1880 cm^{-1} characteristic of nitrosyl species resulting from oxidation of adsorbed ammonia [29, 38, 51]. This wavenumber range corresponds to stretching vibrations of the NO-group, whatever cations it could be bound to: Ru^{4+} and/or W^{6+} [52]. But the peak shift to lower wavenumbers from 1880 cm^{-1} on the spectrum of WO_3-300/Ru to 1860 cm^{-1} on the spectra of WO_3-450/Ru and WO_3-600/Ru (Fig. 16) indicates π-back donation and suggests preferential NO binding to the cations which have more d-electrons, i.e. to the ruthenium cations. Matching with the sensitivity data (Fig. 9), it can be claimed that high sensor response is provided by the Ru-catalyzed NH_3 oxidation. Since neither the participation of OH-groups, nor W-O bonds cleavage

were observed on DRIFT spectra of WO_3/Ru, this reaction assumingly involves surface oxygen species, as indirectly supported by TPR data (Fig. 5):

$$2\ NH_3 + (5/x)\ O_x^- + 2\ Ru = 2\ Ru\text{-}NO + 3\ H_2O + (5/x)\ e^- \qquad (7).$$

The role of the WO_3/Ru microstructure is rationalized by the interplay of chemisorption and oxidation processes. Due to a higher BET area and surface acidity of the matrix obtained at 300 ^{0}C, ammonia was likely too strongly chemisorbed on WO_3-300/Ru (Fig. 16). As a result, the formation of inactive species, e.g. NH_4^+, would impede the oxidation reaction (7). On the other hand, the spectrum of WO_3-450/Ru showed comparable peak intensity for oxidized (N-O 1870 cm^{-1}) and adsorbed (NH_4^+ 1410 cm^{-1}, NH_3 1230 – 1260 cm^{-1}) ammonia species. Hence, the higher sensitivity of this sample to NH_3 is accounted for by balanced impacts from adsorption and oxidation of the target molecules on the sensing process. It completely agrees with what we demonstrated for sulfated tin oxide-based sensors [29]. With further increase in WO_3 particle size, the samples WO_3/Ru possessed lower NH_3 adsorption (WO_3-600/Ru) up till the absence of interaction (WO_3-800/Ru) (Fig. 16), most probably due to the coarsening microstructure.

Conclusions

Tungsten oxide with variable particle size and BET area was obtained via tungstic acid deposition and heat treatment. Its surface was modified with 1 wt.% Pd and Ru by impregnation. The effect of the microstructure and additives on surface sites was investigated. With the growth of the particle size, the content of aqueous species and the surface acidity of WO_3 decreased. Tungsten oxide modification by palladium resulted in materials with improved sensitivity to CO at room temperature. DRIFT spectroscopy revealed that it was due to CO binding to Pd sites on the surface of WO_3/Pd and the adsorbate oxidation by surface aqueous species. No interaction of tungsten oxide with CO at room temperature was detected without the catalytic additive Pd. Modification by ruthenium resulted in an increased concentration of easily reducible species believed to be chemisorbed oxygen. The samples WO_3/Ru were highly sensitive to ammonia at elevated temperature (200 – 250 ^{0}C). The DRIFT study showed that NH_3 adsorption decreased

with increasing WO_3 particle size and was unaffected by noble metal additives. The interaction at raised temperature proceeded differently on blank and modified tungsten oxide. Oxidation of NH_3 on WO_3 involved partial reduction of the oxide inferred from W-O bonds cleavage, implying that the sensing route was as proposed in the oxygen vacancy model. This conclusion was supported by similar observations on tungsten oxide interaction with other reducing gases [26] and can be understood taking into account the tendency of WO_3 structure towards oxygen deficiency. On the other hand, for modified tungsten oxide no traces of bulk reduction were detected. On the surface of WO_3/Ru, adsorbed ammonia was oxidized, producing NO species due to specific catalytic activity of the supported ruthenium. A detrimental influence of the high surface acidity on the sensitivity to NH_3 was shown, and resulted in an imbalance between chemisorption and oxidation processes. The specific promotion of sensitivity to CO and NH_3 by catalytic Pd and Ru additives was found to be based on the same key interaction steps for the presently reported tungsten oxide and previously researched tin oxide-based sensors. Thus, the model of chemical modification by specific catalyst clusters may be considered uniform for different semiconductor metal oxides.

Acknowledgement

This work was supported by ERA-Net.Plus grant N 096 FONSENS.

Supporting Information: Dynamic resistance response of sensors to CO, NH_3 at different operating temperature and gas concentration; XRF spectra of WO_3/Pd, WO_3/Ru.

References

[1] H. Long, W. Zeng, H. Zhang, Synthesis of WO_3 and its gas sensing: a review, J. Mater. Sci.: Mater. Electron. 26 (2015) 4698–4707.

[2] Z.-F. Huang, J. Song, L. Pan, X. Zhang, L. Wang, J.-J. Zou, Tungsten oxides for photocatalysis, electrochemistry, and phototherapy, Adv. Mater. 27 (2015) 5309–5327.

[3] H. A. Wrledt, The O-W (oxygen-tungsten) system, Bulletin of Alloy Phase Diagrams 10 (1989) 368–384.

[4] G. Wang, Y. Ji, X. Huang, X. Yang, P.-I. Gouma, M. Dudley, Fabrication and characterization of polycrystalline WO_3 nanofibers and their application for ammonia sensing, J. Phys. Chem. B 110 (2006) 23777–23782.

[5] C. Balazsi, L. Wang, E. O. Zayim, I. M. Szilagyi, K. Sedlackova, J. Pfeifer, A. L. Toth, P.-I. Gouma, Nanosize hexagonal tungsten oxide for gas sensing applications, Journal of the European Ceramic Society 28 (2008) 913–917.

[6] A. Staerz, C. Berthold, T. Russ, S. Wicker, U. Weimar, N. Barsan, The oxidizing effect of humidity on WO_3 based sensors, Sens. Actuators B 237 (2016) 54–58.

[7] A. M. Korduban, A. P. Shpak, M. M. Medvedskij, Electronic structure exploration of active element surface for hydrogen sensor based on WO_{3-x} nanoparticles. In: T. N. Veziroglu et. al. (eds.), Hydrogen Materials Science and Chemistry of Carbon Nanomaterials. NATO Security through Science Series A: Chemistry and Biology. Springer, Dordrecht. 2007, 59–64.

[8] A. Ponzoni, V. Russo, A. Bailini, C. S. Casarib, M. Ferroni, A. Li Bassi, A. Migliori, V. Morandi, L. Ortolani, G. Sberveglieri, C. E. Bottani, Structural and gas-sensing characterization of tungsten oxide nanorods and nanoparticles, Sens. Actuators B 153 (2011) 340–346.

[9] H. Xia, Y. Wang, F. Kong, S. Wang, B. Zhu, X. Guo, J. Zhang, Y. Wang, S. Wu, Au-doped WO_3-based sensor for NO_2 detection at low operating temperature, Sens. Actuators B 134 (2008) 133–139.

[10] A. T. Mane, S. B. Kulkarni, S. T. Navale, A. A. Ghanwat, N. M. Shinde, J. H. Kim, V. B. Patil, NO_2 sensing properties of nanostructured tungsten oxide thin films, Ceramics International 40 (2014) 16495–16502.

[11] B. Timmer, W. Olthuis, A. van den Berg, Ammonia sensors and their applications—a review, Sens. Actuators B 107 (2005) 666–677.

[12] C. Balazsi, K. Sedlackova, J. Pfeifer, A. L. Toth, E. O. Zayim, I. M. Szilagyi, L. Wang, K. Kalyanasundaram, P.-I. Gouma, Synthesis and examination of hexagonal tungsten oxide nanocrystals for electrochromic and sensing applications, In: M.-I. Baraton (ed.), Sensors for Environment, Health and Security. NATO Science for Peace and Security Series C: Environmental Security. Springer, Dordrecht. 2009, 77–91.

[13] B. T. Marquis, J. F. Vetelino, A semiconducting metal oxide sensor array for the detection of NO_x and NH_3, Sens. Actuators И77 (2001) 100–110.

[14] Y. M. Zhao, Y. Q. Zhu, Room temperature ammonia sensing properties of $W_{18}O_{49}$ nanowires, Sens. Actuators B 137 (2009) 27–31.

[15] A. A. Tomchenko, V. V. Khatko, I. L. Emelianov, WO_3 thick-film gas sensors, Sens. Actuators B 46 (1998) 8–14.

[16] J. Kukkola, J. Maklin, N. Halonen, T. Kyllonen, G. Toth, M. Szabo, A. Shchukarev, J.-P. Mikkola, H. Jantunen, K. Kordas, Gas sensors based on anodic tungsten oxide, Sens. Actuators B 153 (2011) 293–300.

[17] M. Epifani, E. Comini, R. Diaz, A. Genç, J. Arbiol, T. Andreu, P. Siciliano, G. Faglia, J. R. Morante, Surface modification, heterojunctions, and other structures: composing metal oxide nanocrystals for chemical sensors, In: F. H. Teherani, D. C. Look, D. J. Rogers (eds.), Oxide-based Materials and Devices VI. Proc. of SPIE. 9364 (2015) 936415(1–5).

[18] M. Righettoni, A. Tricoli, S. Gass, A. Schmid, A. Amann, S. E. Pratsinis, Breath acetone monitoring by portable Si:WO_3 gas sensors, Analytica Chimica Acta 738 (2012) 69–75.

[19] M. Righettoni, A. Tricoli, S. E. Pratsinis, Si:WO_3 sensors for noninvasive diabetes diagnosis by breath analysis, 2010 IEEE Sensors, Kona, HI, 2010, pp. 1491–1495.

[20] M. Righettoni, A. Tricoli, Toward portable breath acetone analysis for diabetes detection, J. Breath Res. 5 (2011) 037109 (8pp).

[21] A. Staerz, U. Weimar, N. Barsan, Understanding the Potential of WO_3 Based Sensors for Breath Analysis, Sensors 16 (2016) 1815(16pp.).

[22] Y. Zhou, G. Liua, X. Zhu, Y. Guo, Ultrasensitive NO_2 gas sensing based on rGO/MoS_2 nanocomposite film at low temperature, Sens. Actuators B 251 (2017) 280–290.

[23] X. Zhu, Y. Guo, H. Ren, C. Gao, Y. Zhou, Enhancing the NO_2 gas sensing properties of rGO/SnO_2 nanocomposite films by using microporous substrates, Sens. Actuators B 248 (2017) 560–570.

[24] Y. Zhou, C. Gao, Y. Guo, UV assisted ultrasensitive trace NO_2 gas sensing based on few-layer MoS_2 nanosheet–ZnO nanowire heterojunctions at room temperature, J. Mater. Chem. A 6 (2018) 10286–10296.

[25] R. Godbole, V. P. Godbole, S. Bhagwat, Surface morphology dependent tungsten oxide thin films as toxic gas sensor, Materials Science in Semiconductor Processing 63 (2017) 212–219.

[26] M. Hubner, C. E. Simion, A. Haensch, N. Barsan, U. Weimar, CO sensing mechanism with WO_3 based gas sensors, Sens. Actuators B 151 (2010) 103–106.

[27] B. Frtihberger, M. Grunze, D. J. Dwyer, Surface chemistry of H_2S-sensitive tungsten oxide films, Sensors and Actuator B 31 (1996) 167–174.

[28] M. N. Rumyantseva, A. M. Gaskov, Chemical modification of nanocrystalline metal oxides: effect of the real structure and surface chemistry on the sensor properties, Rus. Chem. Bull. Int. Ed. 57 (2008) 1106–1125.

[29] A. Marikutsa, A. Sukhanova, M. Rumyantseva, A. Gaskov, Acidic and catalytic co-functionalization for tuning the sensitivity of sulfated tin oxide modified by ruthenium oxide to ammonia gas, Sens. Actuators B 255 (2018) 3523–3532.

[30] F. Meng, H. Zheng, Y. Chang, Y. Zhao, M. Li, C. Wang, Y. Sun, J. Liu, One-Step Synthesis of Au/SnO_2/RGO Nanocomposites and Their VOC Sensing Properties, IEEE T Nanotechnol. 17 (2018) 212–219.

[31] F. Meng, H. Zheng, Y. Sun, M. Li, J. Liu, Trimethylamine Sensors Based on Au-Modified Hierarchical Porous Single-Crystalline ZnO Nanosheets, Sensors 17(7) (2017) 1478(13 p.)

[32] F. Meng, N. Hou, Z. Jin, B. Sun, W. Li, X. Xiao, C. Wang, M. Li, J. Liu, Sub-ppb detection of acetone using Au-modified flower-like hierarchical ZnO structures, Sens. Actuators B 219 (2015) 209–217.

[33] F. Meng, N. Hou, Z. Jin, B. Sun, Z. Guo, L. Kong, X. Xiao, H. Wu, M. Li, J. Liu, Ag-decorated ultra-thin porous single-crystalline ZnO nanosheets prepared by sunlight induced solvent reduction and their highly sensitive detection of ethanol, Sens. Actuators B 209 (2015) 975–217.

[34] A. V. Marikutsa, M. N. Rumyantseva, L. V. Yashina, A. M. Gaskov, Role of surface hydroxyl groups in promoting room temperature CO sensing by Pd-modified nanocrystalline SnO_2, J. Solid State Chem. 183 (2010) 2389–2399.

[35] A. V. Marikutsa, M.N. Rumyantseva, A. M. Gaskov, E. A. Konstantinova, D. A. Grishina, D. M. Deygen, CO and NH_3 sensor properties and paramagnetic centers of nanocrystalline SnO_2 modified by Pd and Ru, Thin Solid Films 520 (2011) 904–908.

[36] A. V. Marikutsa, M. N. Rumyantseva, E. A. Konstantinova, T. B. Shatalova, A. M. Gaskov, Active sites on nanocrystalline tin dioxide surface: effect of palladium and ruthenium oxides clusters, J. Phys. Chem. C 118 (2014) 21541–21549.

[37] A. Marikutsa, M .Rumyantseva, A. Gaskov, Selectivity of catalytically modified tin dioxide to CO and NH_3 gas mixtures, Chemosensors 3 (2015) 241–252.

[38] A. Marikutsa, M. Rumyantseva, A. Gaskov, Specific interaction of PdO_x- and RuO_y-modified tin dioxide with CO and NH_3 gases: Kelvin probe and DRIFT studies, J. Phys. Chem. C 119 (2015) 24342–24350.

[39] S. Supothina, P. Seeharaj, S. Yoriya, M. Sriyudthsak, Synthesis of tungsten oxide nanoparticles by acid precipitation method, Ceramics International 33 (2007) 931–936.

[40] A. Marikutsa, M. Rumyantseva, D. Frolov, I. Morozov, A. Boltalin, A. Fedorova, I. Petukhov, L. Yashina, E. Konstantinova, E. Sadovskaya, et al. Role of PdO_x and RuO_y clusters in oxygen exchange between nanocrystalline tin dioxide and the gas phase, J. Phys. Chem. C 117 (2013) 23858–23867.

[41] G. Gao, W. Feng, G. Wu, J. Shen, Z. Zhang, X. Jin, Z. Zhang, A. Du, An investigation on the assembling of WO_3 particles on the matrix of silica solution, J. Sol-Gel Sci. Technol. 64 (2012) 427–435.

[42] G. N. Kustova, Yu. A. Chesalov, L. M. Plyasova, I. Yu. Molin, A. I. Nizovskii, Vibrational spectra of $WO_3 \cdot nH_2O$ and WO_3 polymorphs, Vibrational Spectroscopy 55 (2011) 235–240.

[43] A. Antonaia, M. C. Santoro, G. Fameli, T. Polichetti, Transport mechanism and IR structural characterisation of evaporated amorphous WO_3 films, Thin Solid Films 426 (2003) 281–287.

[44] N. Barsan, M. Schweizer-Berberich, W. Göpel, Fundamental and practical aspects in the design of nanoscaled SnO_2 gas sensors: a status report, Fresenius J. Anal. Chem. 365 (1999) 287–304.

[45] M. Rumyantseva, V. Kovalenko, A. Gaskov, E. Makshina, V. Yuschenko, I. Ivanova, A. Ponzoni, G. Faglia, E. Comini, Nanocomposites SnO_2/Fe_2O_3: Sensor and catalytic properties, Sens. Actuators B 118 (2006) 208–214.

[46] V. Khatko, E. Llobet, X. Vilanova, J. Brezmes, J. Hubalek, K. Malysz, X. Correig, Gas sensing properties of nanoparticle indium-doped WO_3 thick films, Sens. Actuators B 111–112 (2005) 45–51.

[47] K. I. Hadjiivanov, G. N. Vayssilov, Characterization of oxide surfaces and zeolites by carbon monoxide as an IR probe molecule, Adv. Catal. 47 (2002) 307–511.

[48] C. Y. Liu, K. Aika, Ammonia adsorption on ion-exchanged Y-zeolites as ammonia storage material, Journal of the Japan Petroleum Institute 46 (2003) 301–307.

[49] M. Trombetta, G. Ramis, G. Busca, B. Montanari, A. Vaccar, Ammonia adsorption and oxidation on Cu/Mg/Al mixed oxide catalysts prepared via hydrotalcite-type precursors, Langmuir 13 (1997) 4628-4637.

[50] I. Onal, S. Soyer, S. Senkan, Adsorption of water and ammonia on TiO_2-anatase cluster models, Surface Science 600 (2006) 2457–2469.

[51] A. Boccuzzi, E. Guglielminotti, IR Study of TiO_2-based Gas-sensor Materials: Effect of Ruthenium on the Oxidation of NH_3, $(CH_3)_3N$ and NO, Sens. Actuators B 21 (1994) 27–31.

[52] K. I. Hadjiivanov, Identification of neutral and charged N_xO_y surface species by IR spectroscopy. Catal. Rev. – Sci. Eng. 42 (2000) 71–144.

Author biographies

Artem Marikutsa received his PhD in chemistry in 2012 from the Chemistry department of Moscow State University. Researcher at the Laboratory of Semiconductor and Sensor Materials, Moscow State University (2011 – 2017), assistant professor at the Inorganic chemistry division, Chemistry department, Moscow State University (2017 – present time). Research is focused on nanocrystalline gas sensitive materials based on semiconductor metal oxides, study of gas-solid interactions, surface sites and chemical modification.

Lili Yang is currently a PhD student at Chemistry department, Moscow State University. Research work is performed at the Laboratory of Semiconductor and Sensor Materials and focused on the nanocrystalline tungsten oxide-based gas sensors.

Marina Rumyantseva received her PhD in chemistry in 1996 from Moscow State University and Grenoble Polytechnic Institute, her doctoral degree in chemistry in 2009 from the Chemistry department of Moscow State University. Since 2013 she is a professor and a head of the sensor group at the Laboratory of Semiconductor and Sensor Materials, Moscow State University. Her research activities include synthesis and modification of nanostructural materials for gas sensing, investigation of surface and bulk chemistry of nanocrystalline gas sensitive materials and photosensibilization of semiconductor gas sensors.

Maria Batuk is a Post-Doc researcher at the University of Antwerp, Department of Physics, Electron Microscopy for Materials Science. Her research includes the investigation of atomic composition, microstructure and morphology of complex inorganic compounds and emerging functional materials (for energetics, photovoltaics, sensors etc.) using advanced electron microscopy techniques.

Joke Hadermann is a Physics Professor at the University of Antwerp. Her research is centered on the use of advanced transmission electron microscopy techniques for the structure solution (at atomic, nano and micro scale) of new materials, mainly perovskite based and lithium battery

materials, but also thin films photovoltaics, hydrogen storage materials, sensors and complex mixed anion compounds.

Alexander Gaskov received his PhD in chemistry in 1969 and his doctoral degree in chemistry in 1988 from the Chemistry department of Moscow State University. Since 1992 he is a full professor at the Chemistry department of Moscow State University. He is the head of Laboratory of Semiconductor and Sensor Materials in Moscow State University. His scientific interests cover nanostructured semiconductor materials, thin films, quantum dots and nanocomposites for the applications in gas sensing, optical devices and medical diagnostics.

Figure captions

Figure 1. XRD patterns of pristine and modified tungsten oxide samples based on WO_3 obtained at 800 ^{0}C (*a*), 600 ^{0}C (*b*), 450 ^{0}C (*c*) and 300 ^{0}C (*d*). Peaks are indexed for low-temperature monoclinic WO_3 phase (JCPDS 43-1035).

Figure 2. TEM images with inserted electron diffraction patterns corresponding either to [100] or [010] orientation of monoclinic WO_3 (*a, b*), Overview HAADF-STEM images (*c, d*), and STEM-EDX elemental maps: blue – W, green – Pd, red - Ru (*e, f*) of the samples: WO_3-300/Pd (*a, c, e*) and WO_3-450/Ru (*b, d, f*).

Figure 3. XPS spectra of Pd 3d signal from WO_3-300/Pd (*a*) and Ru 3d signal from WO_3-450/Ru (*b*) samples.

Figure 4. FTIR spectra of pristine and modified tungsten oxide samples based on WO_3 annealed at 300 ^{0}C (*a*), 450 ^{0}C (*b*), 600 ^{0}C (*c*) and 800 ^{0}C (*d*).

Figure 5. Temperature profiles of reduction by hydrogen for samples WO_3 (*a*), WO_3/Pd (*b*) and WO_3/Ru (*c*) based on tungsten oxide prepared at different annealing temperatures.

Figure 6. Temperature profiles of ammonia desorption from WO_3 samples obtained at different annealing temperature.

Figure 7. Dynamic response of sensors based on WO_3-300/Pd to 20 ppm CO at room temperature (*a*) and WO_3-450/Ru to 20 ppm NH_3 at 200 ^{0}C (*b*). Response (t_{res}) and recovery (t_{rec}) time intervals are highlighted.

Figure 8. Logarithm of sensor signals to CO (20 ppm) for blank and modified tungsten oxide in relation to annealing temperature of WO_3 matrix and operating temperature of sensors.

Figure 9. Logarithm of sensor signals to NH_3 (20 ppm) for blank and modified tungsten oxide in relation to annealing temperature of WO_3 matrix and operating temperature of sensors.

Figure 10. Comparison of sensor signals to 20 ppm CO at room temperature (*a*) and to 20 ppm NH_3 at 200 ^{0}C (*b*) for sensors based on pristine, Pd- and Ru-modified nanocrystalline oxides WO_3, SnO_2 and In_2O_3 in relation to their average particle size. The *n*-type MOS matrices were obtained by aqueous deposition of metal hydroxides and annealed at different temperatures in the range 300 – 1000 ^{0}C.

Figure 11. Sensor signal of WO_3-300/Pd to CO at room temperature (*a*) and of WO_3-450/Ru to NH_3 at 200 ^{0}C (*b*) in relation to target gas concentration measured under different percentage of relative humidity.

Figure 12. Sensor signals of four samples of pristine tungsten oxide (WO_3-300, WO_3-450) and modified tungsten oxide (WO_3-300/Pd, WO_3-450/Ru) to 10 ppm of different inorganic target gases in dry air. Operation temperature of sensors: WO_3-300, WO_3-450 – 300 ^{0}C, WO_3-450/Ru – 200 ^{0}C, WO_3-300/Pd – room temperature.

Figure 13. DRIFT spectra of WO_3, WO_3/Pd and WO_3/Ru samples based on tungsten oxide obtained at different annealing temperature under the exposure to 200 ppm CO for 1 h at 30 ^{0}C. Inset shows enlarged band of stretching carbonyl vibrations.

Figure 14. DRIFT spectra of WO_3, WO_3/Pd and WO_3/Ru samples based on tungsten oxide obtained at different annealing temperature under the exposure to 200 ppm NH_3 for 1 h at 30 ^{0}C.

Figure 15. DRIFT spectra of samples exposed to 200 ppm NH_3 for 1 h at 200 ^{0}C for: (*a*) pristine WO_3 obtained at different annealing temperature; (*b*) WO_3, WO_3/Pd and WO_3/Ru based on tungsten oxide matrix annealed at 300 ^{0}C; (*c*) WO_3, WO_3/Pd and WO_3/Ru based on tungsten oxide matrix annealed at 450 ^{0}C.

Figure 16. DRIFT spectra of WO_3/Ru samples based on tungsten oxide obtained at different annealing temperature under the exposure to 200 ppm NH_3 for 1 h at 200 ^{0}C.

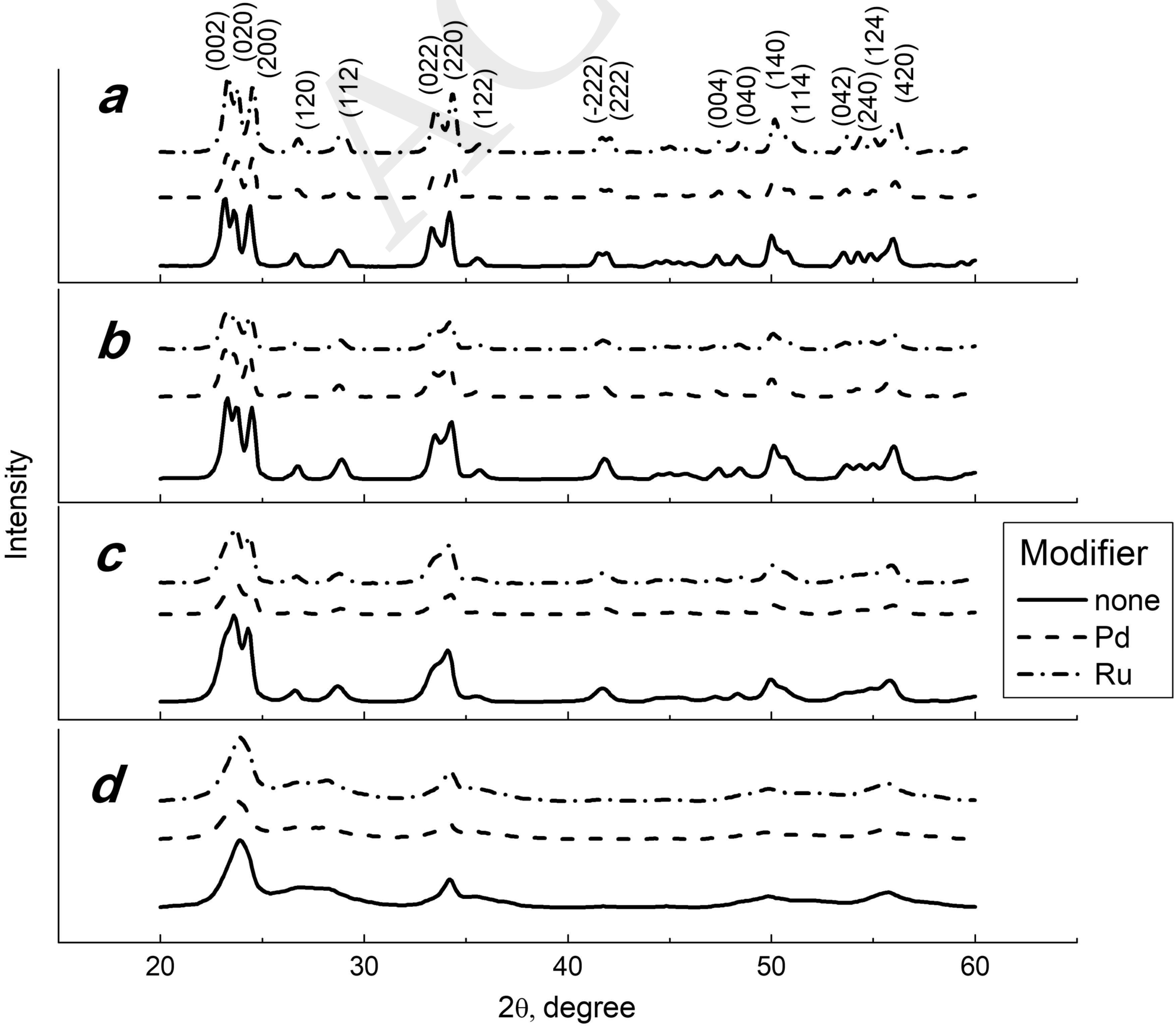
a
b
c
d
(002)
(020)
(200)
(120)
(112)
(022)
(220)
(122)
(-222)
(222)
(004)
(040)
(140)
(114)
(042)
(240)
(124)
(420)
Intensity
20
30
40
50
60
2θ, degree
Modifier
none
Pd
Ru

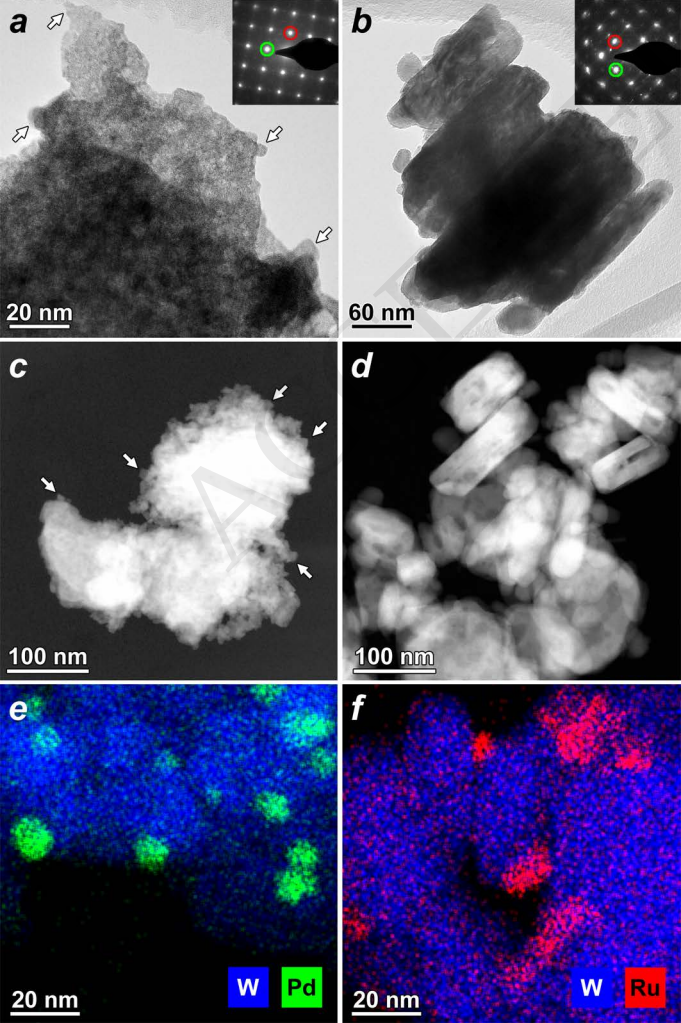
a
20 nm
b
60 nm
c
100 nm
d
100 nm
e
W
Pd
20 nm
f
W
Ru
20 nm

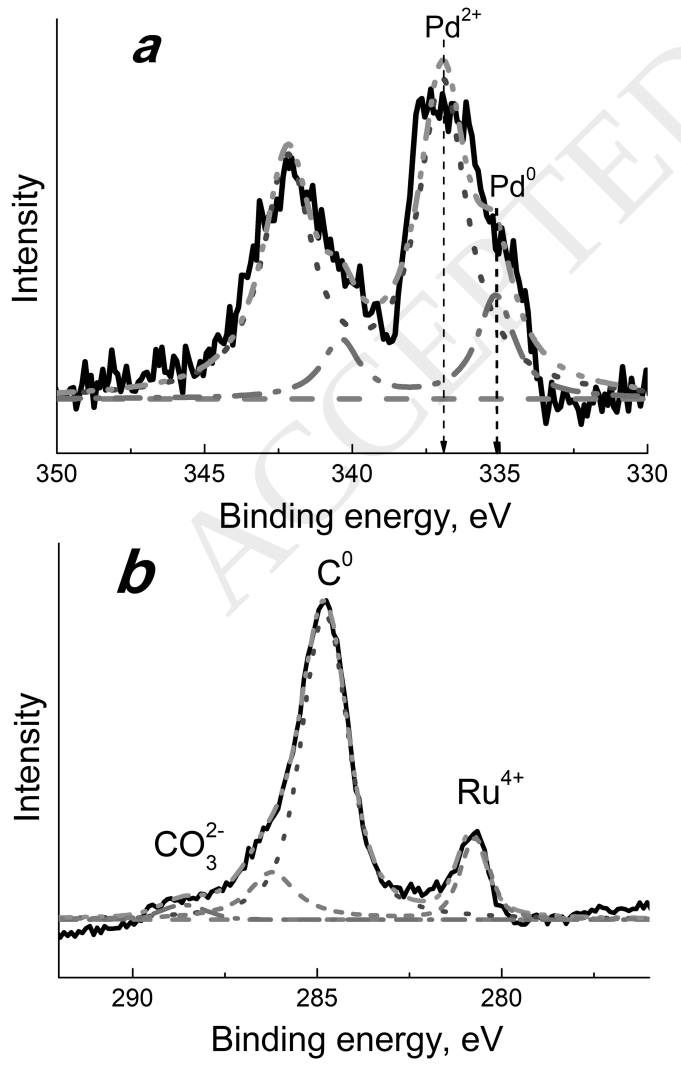
a
Pd2+
Pd0
Intensity
350
345
340
335
330
Binding energy, eV
b
C0
Ru4+
CO3 2-
Intensity
290
285
280
Binding energy, eV

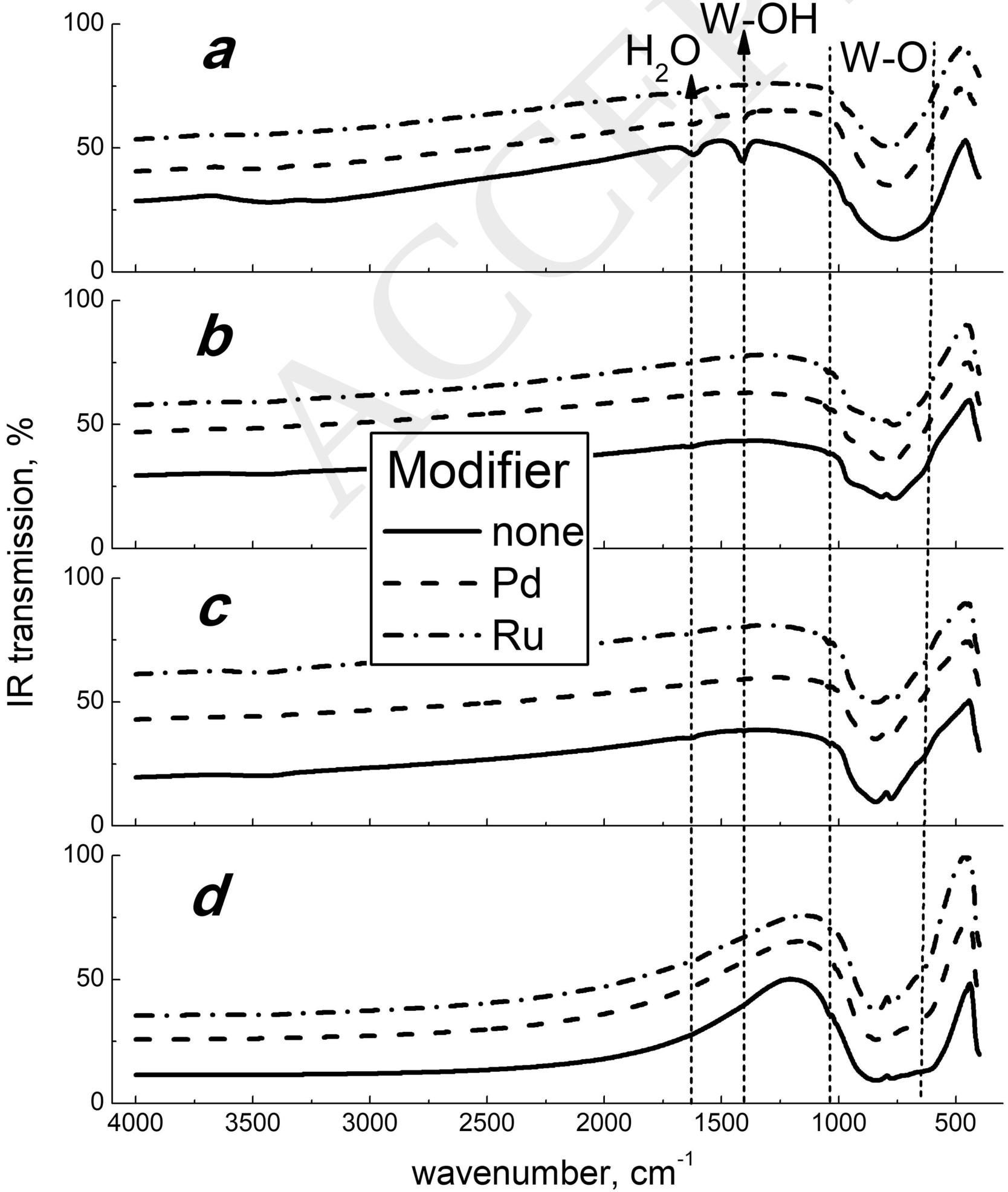
a
b
c
d
W-OH
H2O
W-O
Modifier
none
Pd
Ru
IR transmission, %
wavenumber, cm-1
100
50
0
4000
3500
3000
2500
2000
1500
1000
500

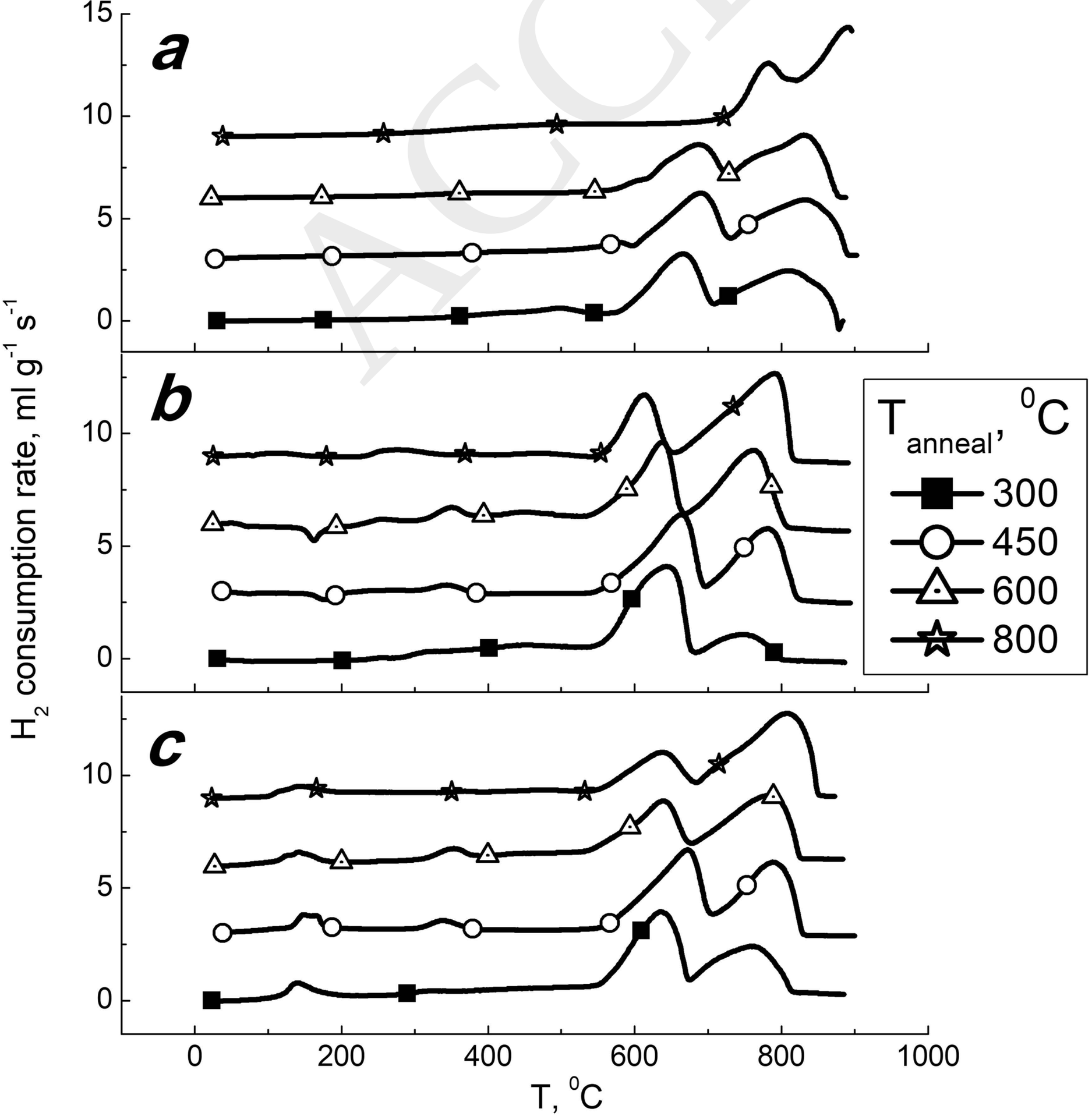
a
b
c
15
10
5
0
0
200
400
600
800
1000
T, ^{0}C
H_2 consumption rate, ml g^{-1} s^{-1}
T_{anneal}, ^{0}C
300
450
600
800

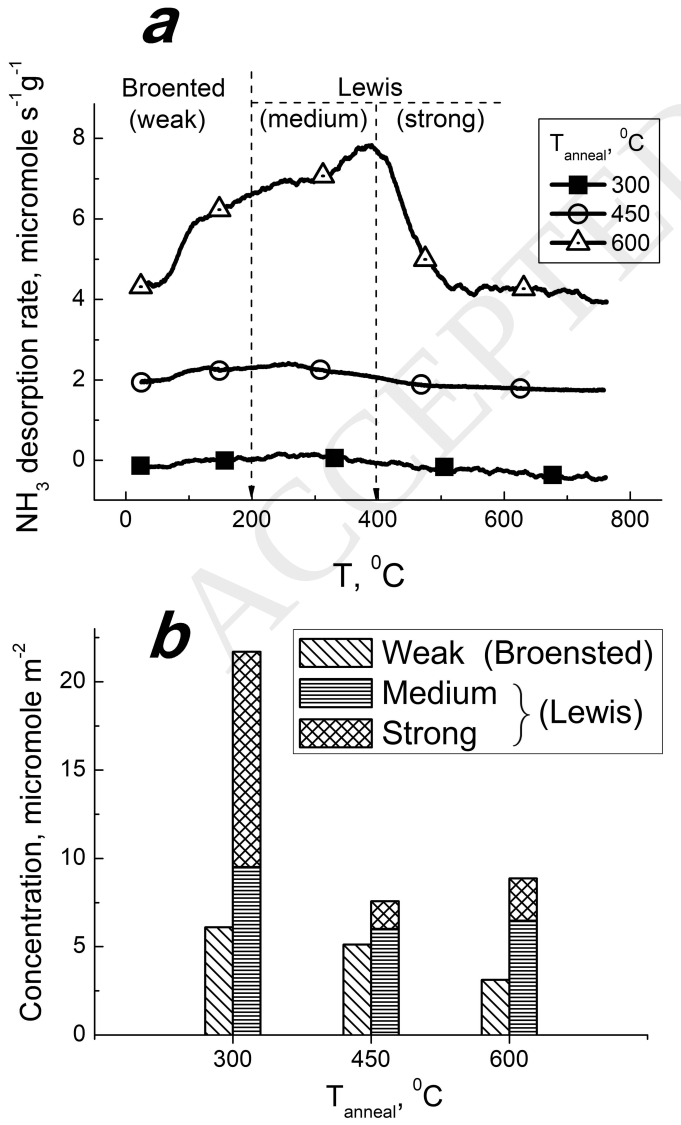
a
Broented
(weak)
Lewis
(medium)
(strong)
T anneal, 0C
300
450
600
NH3 desorption rate, micromole s-1g-1
0
2
4
6
8
0
200
400
600
800
T, 0C
b
Weak (Broensted)
Medium
Strong
(Lewis)
Concentration, micromole m-2
0
5
10
15
20
300
450
600
T anneal, 0C

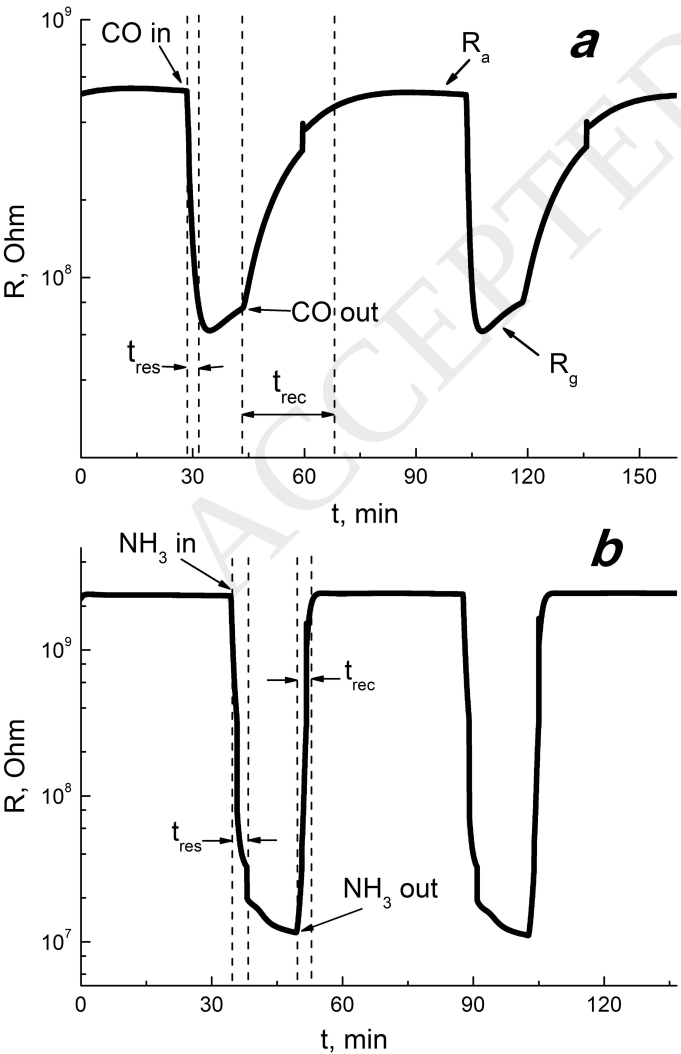
a
CO in
R_a
CO out
R_g
t_res
t_rec
R, Ohm
t, min
b
NH_3 in
t_rec
t_res
NH_3 out
R, Ohm
t, min

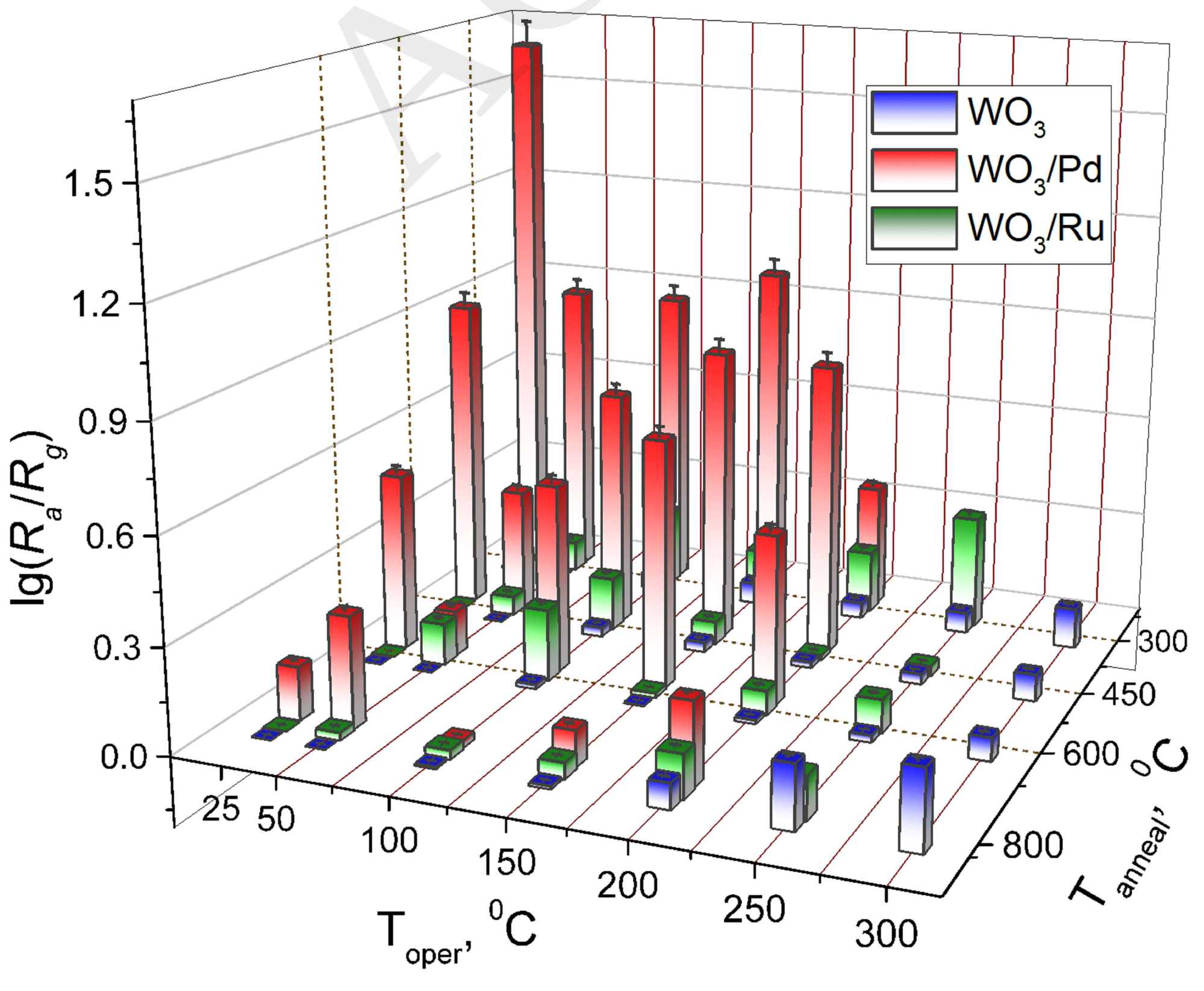
WO3
WO3/Pd
WO3/Ru
lg(Ra/Rg)
1.5
1.2
0.9
0.6
0.3
0.0
25
50
100
150
200
250
300
Toper, 0C
300
450
600
800
Tanneal, 0C

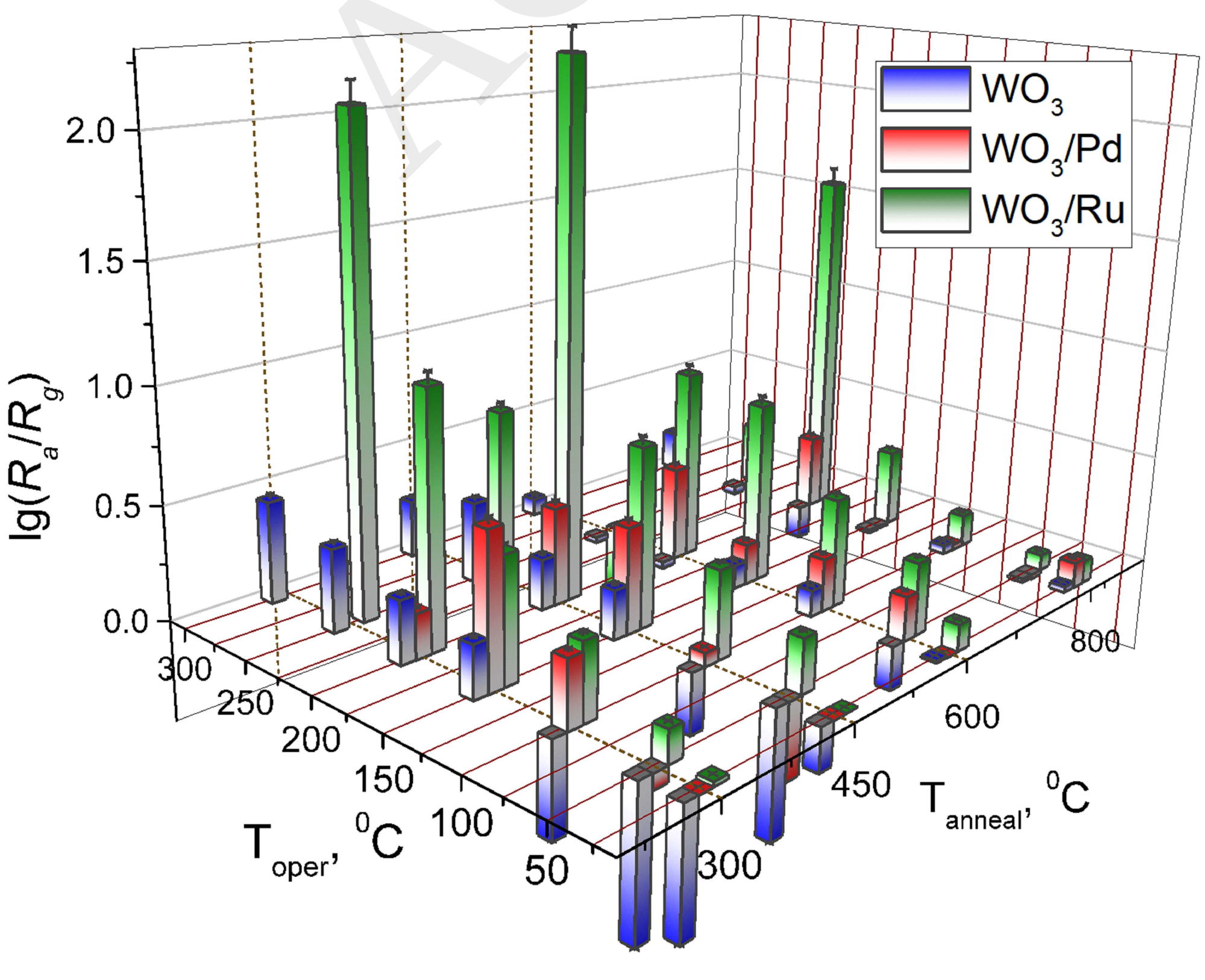
WO3
WO3/Pd
WO3/Ru
lg(Ra/Rg)
2.0
1.5
1.0
0.5
0.0
300
250
200
150
100
50
Toper, 0C
300
450
600
800
Tanneal, 0C

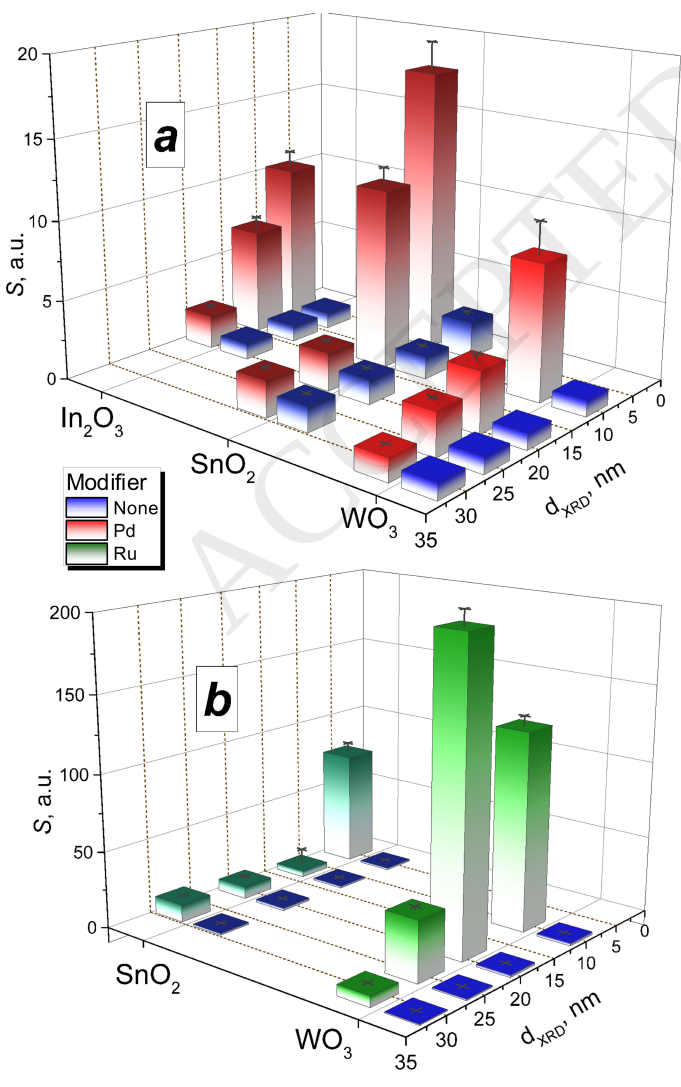
a
S, a.u.
20
15
10
5
0
In2O3
SnO2
WO3
Modifier
None
Pd
Ru
0
5
10
15
20
25
30
35
dXRD, nm
b
S, a.u.
200
150
100
50
0
SnO2
WO3
0
5
10
15
20
25
30
35
dXRD, nm

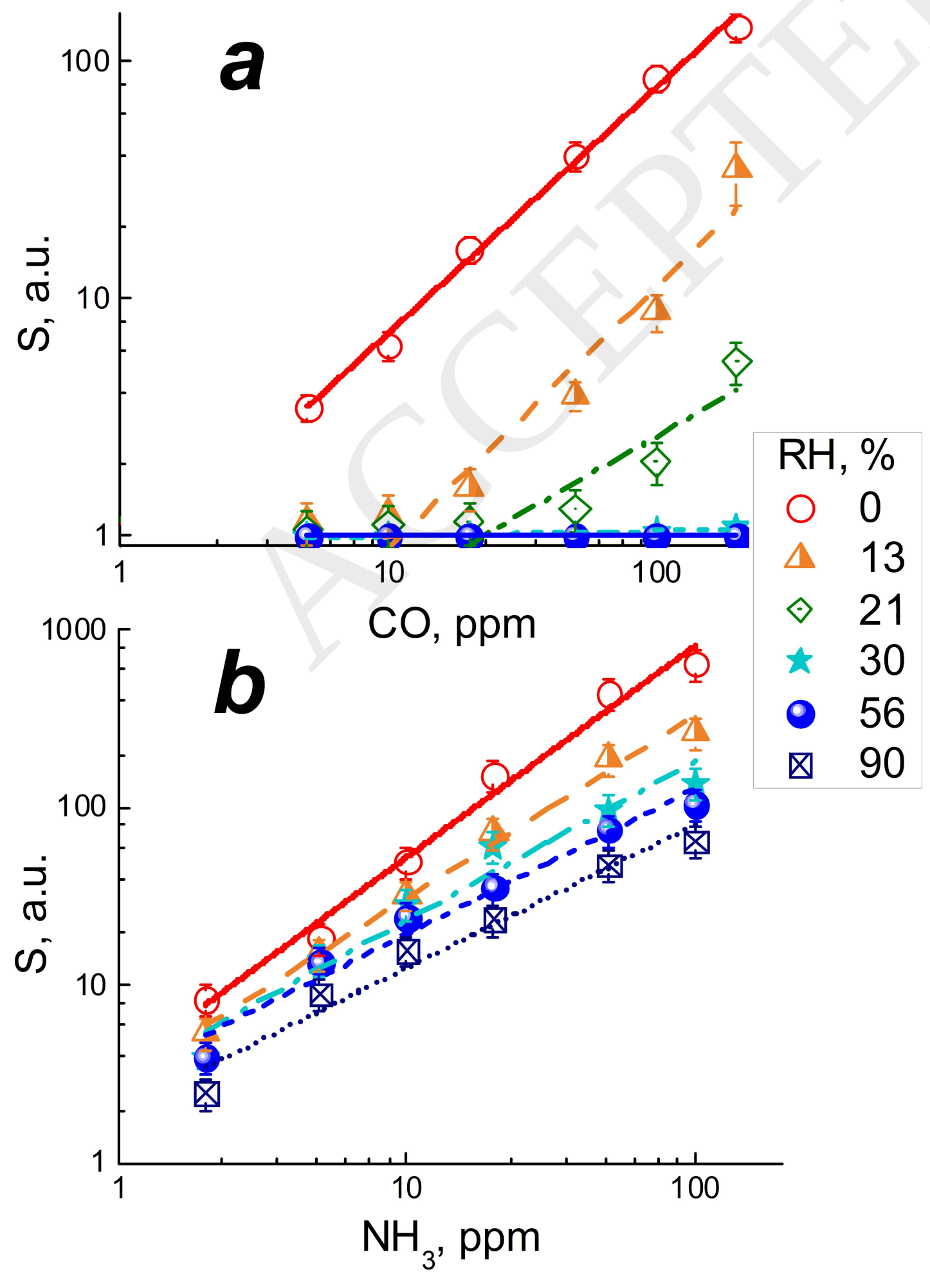
a
100
10
1
S, a.u.
1
10
100
CO, ppm
RH, %
0
13
21
30
56
90
b
1000
100
10
1
S, a.u.
1
10
100
NH3, ppm

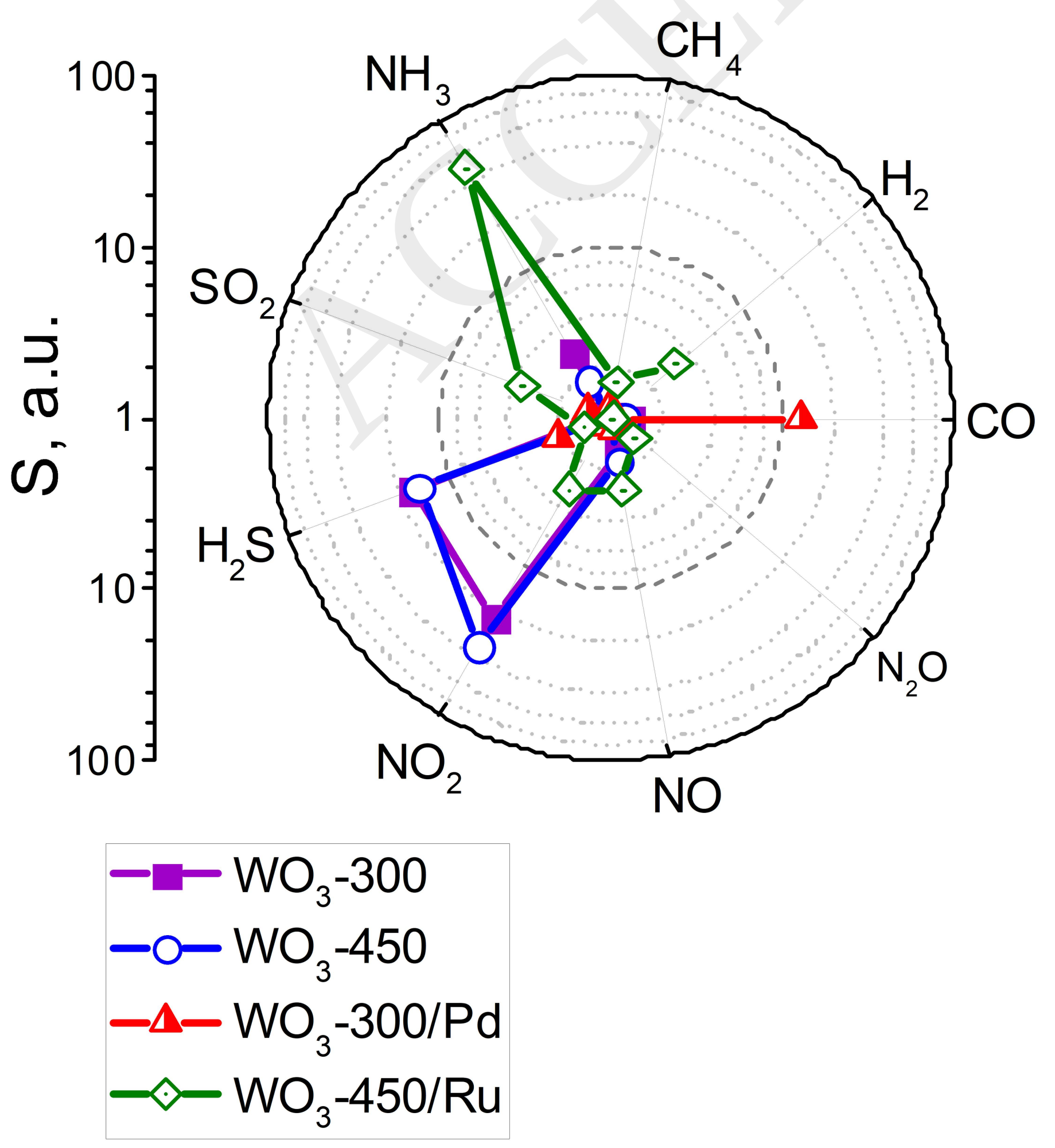
CH4
NH3
H2
SO2
CO
H2S
N2O
NO2
NO
100
10
1
10
100
S, a.u.
WO3-300
WO3-450
WO3-300/Pd
WO3-450/Ru

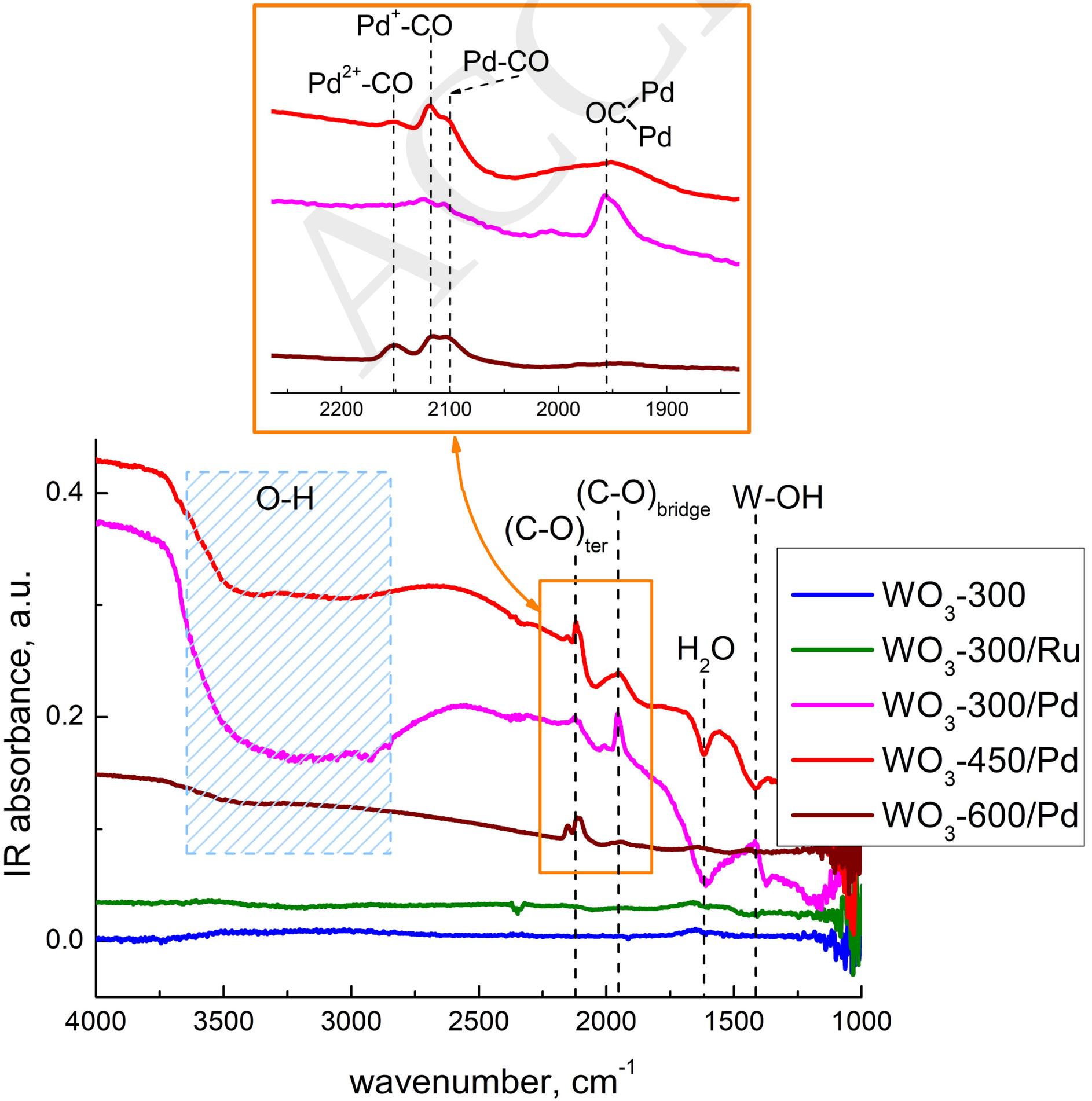
Pd+-CO
Pd2+-CO
Pd-CO
OC
Pd
Pd
2200
2100
2000
1900
O-H
(C-O)bridge
W-OH
(C-O)ter
H2O
WO3-300
WO3-300/Ru
WO3-300/Pd
WO3-450/Pd
WO3-600/Pd
IR absorbance, a.u.
0.4
0.2
0.0
4000
3500
3000
2500
2000
1500
1000
wavenumber, cm-1

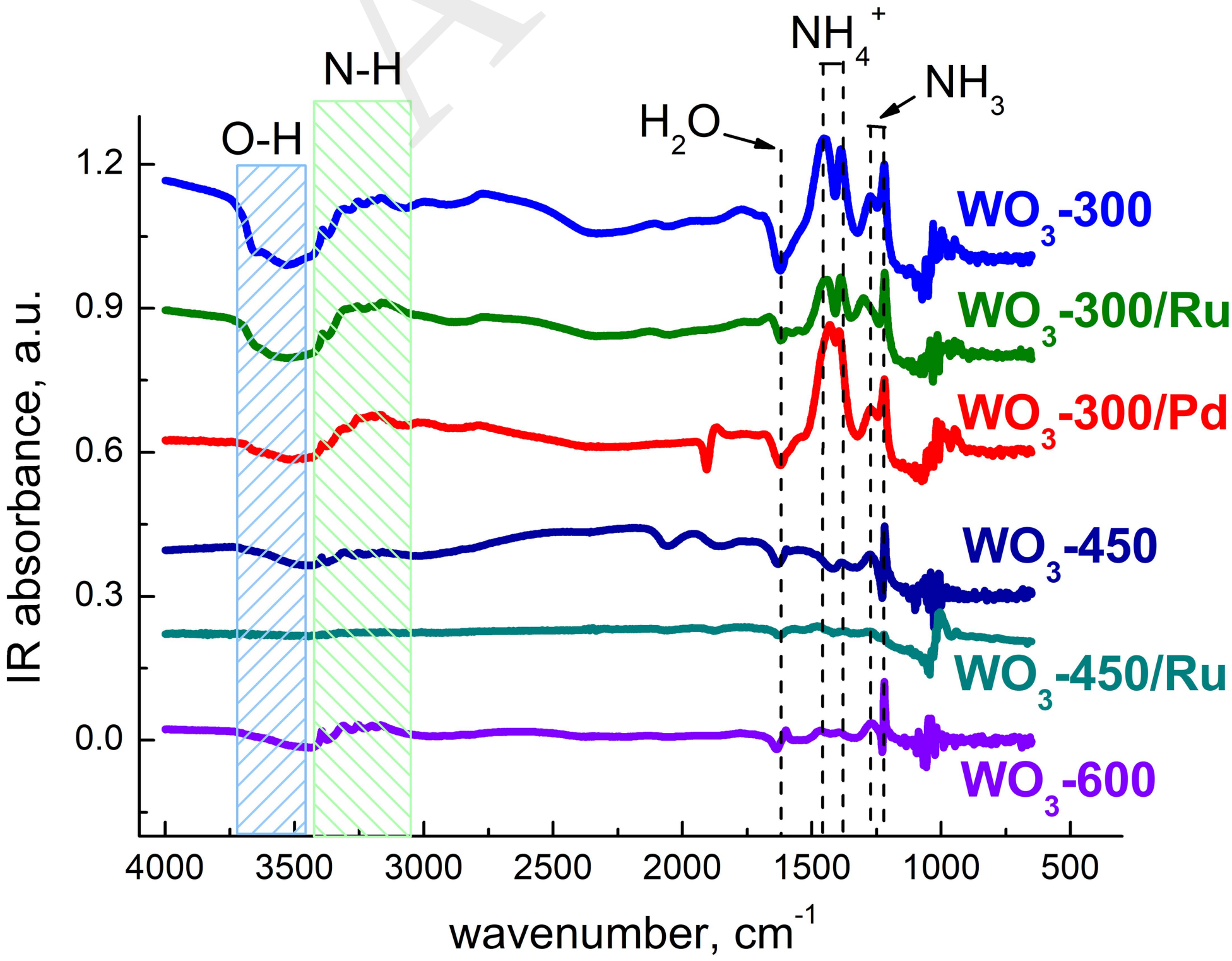
NH4+
N-H
NH3
H2O
O-H
WO3-300
WO3-300/Ru
WO3-300/Pd
WO3-450
WO3-450/Ru
WO3-600
IR absorbance, a.u.
1.2
0.9
0.6
0.3
0.0
4000
3500
3000
2500
2000
1500
1000
500
wavenumber, cm-1

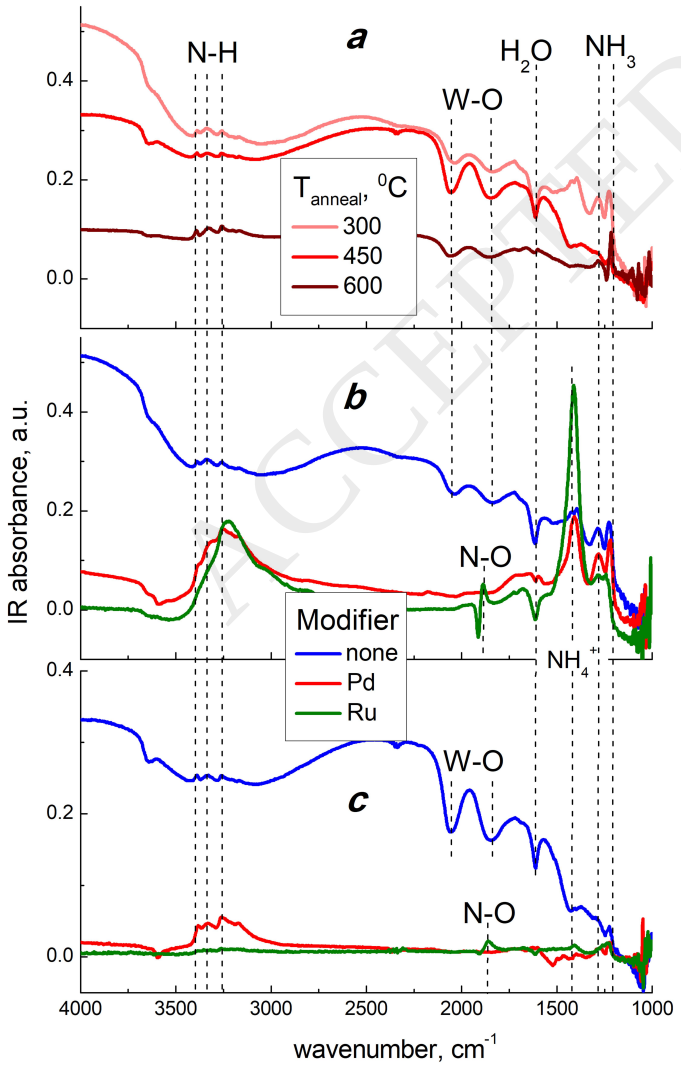
a
b
c
N-H
W-O
H2O
NH3
N-O
NH4+
Tanneal, 0C
300
450
600
Modifier
none
Pd
Ru
IR absorbance, a.u.
wavenumber, cm-1
0.0
0.2
0.4
4000
3500
3000
2500
2000
1500
1000

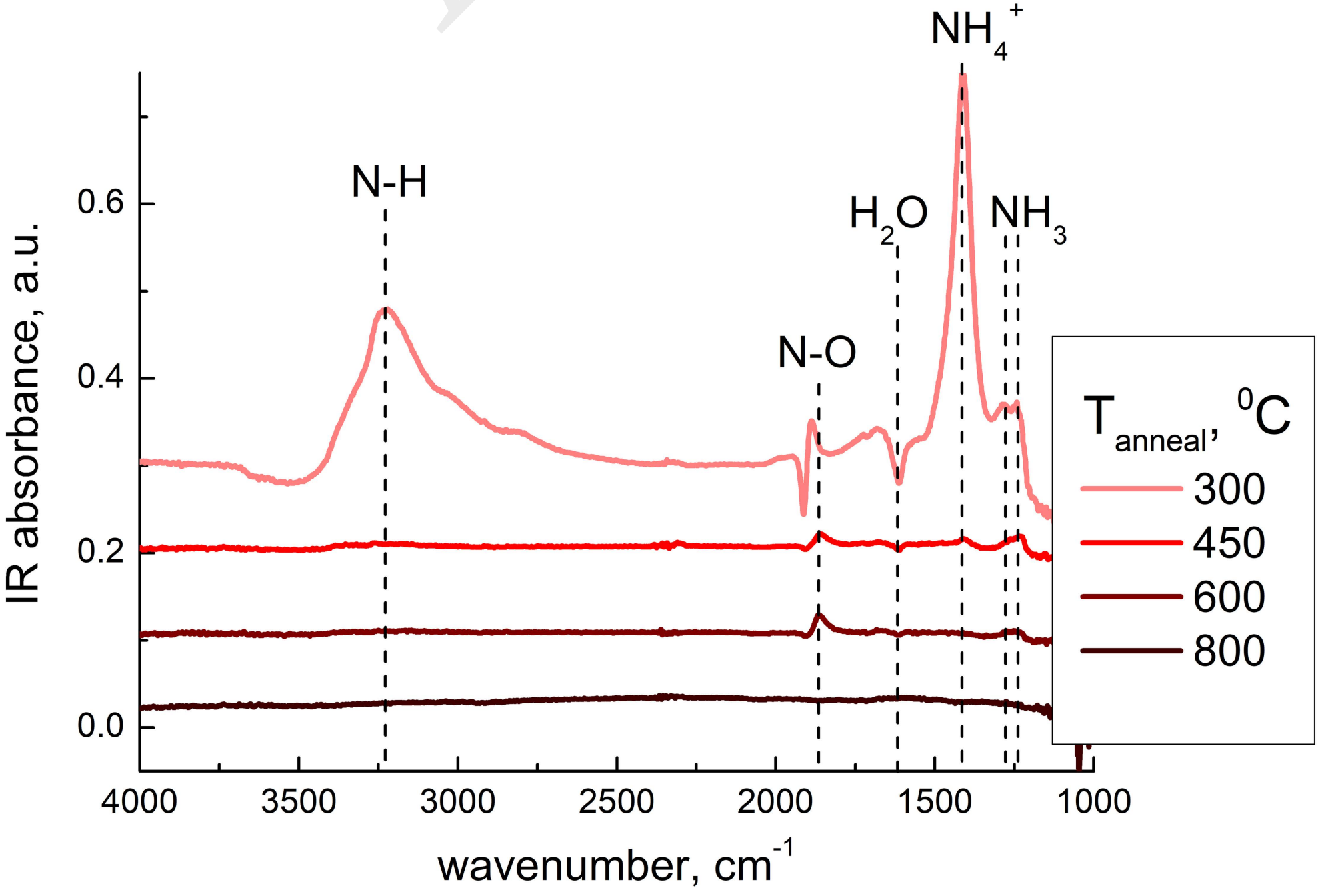
NH4+
N-H
H2O
NH3
N-O
IR absorbance, a.u.
0.6
0.4
0.2
0.0
4000
3500
3000
2500
2000
1500
1000
wavenumber, cm-1
Tanneal, 0C
300
450
600
800

Table 1. Samples designation, composition and microstructure parameters

Designation	Annealing temperature of WO_3, ^0C	Modifier, wt.% (from XRF)	d_{XRD} (WO_3), nm	BET area, m^2/g
WO_3-300	300	-	7.0 – 9.2	25 – 32
WO_3-300/Pd		Pd, 0.95 ± 0.05	7.4 – 9.5	
WO_3-300/Ru		Ru, 1.03 ± 0.05	8.5 – 10.0	
WO_3-450	450	-	19.2 – 21.6	5 – 9
WO_3-450/Pd		Pd, 0.91 ± 0.05	18.1 – 22.0	
WO_3-450/Ru		Ru, 0.97 ± 0.05	18.5 – 21.8	
WO_3-600	600	-	22.8 – 24.7	2 – 4
WO_3-600/Pd		Pd, 1.02 ± 0.05	24.8 – 25.2	
WO_3-600/Ru		Ru, 0.98 ± 0.05	23.8 – 26.0	
WO_3-800	800	-	27.2 – 35.4	< 2
WO_3-800/Pd		Pd, 0.88 ± 0.05	28.5 – 36.7	
WO_3-800/Ru		Ru, 0.90 ± 0.05	27.9 – 34.8	